EMBRY-RIDDLE
Aeronautical University™
SCHOLARLY COMMONS

Aviation Propulsive Lithium-Ion Battery Packs State-of-Charge and State-of-Health Estimations and Propulsive Battery System Weight Analysis

Jingsi Lilly

AVIATION PROPULSIVE LITHIUM-ION BATTERY PACKS

STATE-OF-CHARGE AND STATE-OF-HEALTH ESTIMATIONS

AND PROPULSIVE BATTERY SYSTEM WEIGHT ANALYSIS

A Thesis

Submitted to the Faculty

of

Embry-Riddle Aeronautical University

by

Jingsi Lilly

In Partial Fulfillment of the

Requirements for the Degree

of

Master of Science in Aerospace Engineering

December 2017

Embry-Riddle Aeronautical University

Daytona Beach, Florida

AVIATION PROPULSIVE LITHIUM-ION BATTERY PACKS STATE-OF-CHARGE AND STATE-OF-HEALTH ESTIMATION AND PROPULSIVE BATTERY SYSTEM WEIGHT ANALYSIS
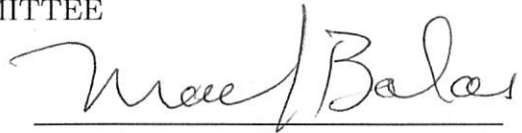
by

Jingsi Lilly

A Thesis prepared under the direction of the candidate's committee chairman, Dr. Richard "Pat" Anderson and co-advisor, Dr. Mark Balas, Department of Aerospace Engineering, and has been approved by the members of the thesis committee. It was submitted to the School of Graduate Studies and Research and was accepted in partial fulfillment of the requirements for the degree of Master of Science in Aerospace Engineering.

THESIS COMMITTEE

_____
Chairman, Dr. Richard "Pat" Anderson

_____
Co-advisor, Dr. Mark Balas

_____
Member, Dr. D. Steven Daniel
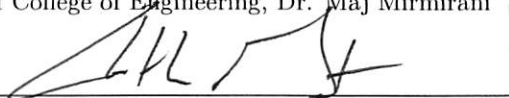
_____
Member, Dr. Richard J. Prazenica

_____
Graduate Program Coordinator, Dr. Magdy Attia

10/6/2017
_____
Date

_____
Dean of College of Engineering, Dr. Maj Mirmirani

10/7/2017
_____
Date

_____
Vice Chancellor, Academic Support, Dr. Christopher Grant

10/9/17
_____
Date

TABLE OF CONTENTS

LIST OF TABLES

LIST OF FIGURES

SYMBOLS

$\underline{b}(n)$	System parameter vector at n^{th} time step (expressed in recursive least squares)
C	Capacitance of the capacitor in the RC parallel circuit
e_{Bat}	A battery cell's available capacity
e_{remain}	A battery cell's remaining energy
$e(n)$	Error at n^{th} time step
E_{Bat}	A battery pack's available capacity
E_m	Open circuit voltage
E_{remain}	A cell unit's remaining energy
$\underline{f}(n)$	System excitations at n^{th} time step (expressed in recursive least squares)
$h(n)$	System excitation at n^{th} time step (expressed in least squares)
H	System excitation matrix (expressed in least squares)
I	Current
R	Resistance of the resistor in the RC parallel circuit
R_0	Internal resistance
V	Terminal voltage
V_{RC}	Voltage across the RC parallel circuit
W_0	Aircraft maximum gross take-off weight
W_{Bat}	Propulsive battery system weight
W_{BMS}	Battery management system weight
W_{Cell}	Propulsive battery cells weight
W_{Cool}	Battery pack cooling system weight
W_{House}	Battery pack housing structures weight
W_{Wire}	Battery pack wiring system weight
w_{Bat}	Propulsive battery system weight fraction
w_{BMS}	Battery management system weight fraction
w_{Cell}	Propulsive battery cells weight fraction
w_{Cool}	Battery pack cooling system weight fraction
w_{House}	Battery pack housing structures weight fraction
w_{Wire}	Battery pack wiring system weight fraction
t_{signal}	Recursive least squares system input signal duration
$t_{converge}$	Recursive least squares converging time
$y(n)$	System measurements at n^{th} time step
Y	System measurement matrix
Z	Battery impedance in general
Z_0	Battery initial impedance

Z_{act}	Battery actual impedance
Z_{EOL}	Battery end-of-life impedance
ϵ_{Bat}	Battery specific energy
ϵ_{Bat_e}	Battery effective specific energy
τ_{RC}	Time constant of the RC parallel circuit
$\theta(n)$	System parameters at n^{th} time step (expressed in least squares)
Θ	System parameter matrix (expressed in least squares)

ABBREVIATIONS

AC	Alternating current
AFM	Airplane flight manual
AWG	American wire gauge
BMS	Battery management system
CG	Center of gravity
DC	Direct current
ECM	Equivalent circuit model
EFRC	Eagle Flight Research Center
EIS	Electrochemical impedance spectroscopy
EKF	Extended Kalman filter
EOL	End of life
ERAU	Embry-Riddle Aeronautical University
EV	Electric vehicle
FAA	Federal Aviation Administration
PMPG	Passenger miles per gallon
GA	General aviation
Li-ion	Lithium-ion
MGTOW	Maximum gross take-off weight
NASA	National Aeronautics and Space Administration
OCV	Open circuit voltage
PCC	Phase change composite
RLS	Recursive least squares
RPM	Revolutions per minute
SOC	State-of-charge
SOH	State-of-health

ABSTRACT

Lilly, Jingsi MSAE, Embry-Riddle Aeronautical University, December 2017. Aviation

Propulsive Lithium-ion Battery Packs State-of-Charge and State-of-Health Estima-

tions And Propulsive Battery System Weight Analysis.

Aviation propulsive battery pack research is in high demand with the development of electric and hybrid aircraft. Accurate in-flight state-of-charge and state-of-health estimations of aviation battery packs still remain challenging. This thesis puts efforts on estimating the state-of-charge, state-of-health, and remaining energy of a lithium-ion propulsive battery pack with a recursive least squares based adaptive estimator. By reading the system measurements (discharging currents and terminal voltages) with persistent excitation, the proposed estimator can determine the present internal parameters of the battery cells and further interpolate them into state-of-charge, state-of-health, and the remaining energy information. The validation results indicate that the recursive least squares based estimator achieves convergence within a very short time period ($\approx$ 1 second) with desirable estimation accuracy (normally under 1%).

To validate the recursive least squares based estimator, a lithium-ion single cell simulation model is developed to simulate a NCR18650GA single cell's performance during discharge at 25°C. Validations of the single cell simulation model with both constant discharging current and HK-36 flight mission profile show simulation errors less than 1.3%.

This thesis also empirically analyzes the propulsive battery system weight and weight fractions based on the HK-36 electric airplane propulsive battery system designing experiences. As a result, the entire HK-36 propulsive battery system takes approximately 27% of the aircraft gross weight. 58% of the battery system weight is the cells' weight, and 42% is the auxiliary components weight. Taking the weight fraction into consideration, NCR18650GA cells' effective specific energy reduces from 0.16 HP-hr/lb (259 W-hr/kg) to 0.09 HP-hr/lb (150 W-hr/kg).

1. Introduction

1.1 Background

The aviation industry has been using fuel (such as 100LL and JetA) as the main propulsive energy source since the 20th century. Traditional fuel-burning aviation engines are accompanied by numerous environmental problems, such as green house gas (CO_2) emissions and noise pollution. Based on the published data from the U.S. Energy Information Administration (EIA), aviation fuels (aviation gasoline and jet fuel) account for approximately 12% of the total energy the U.S. transportation sector used in 2016 (United States Energy Information Administration, 2017). The use of fuels will keep increasing with the growth of the aviation industry. The Federal Aviation Administration (FAA) forecasts that general aviation flying hours will increase an average of 0.9% per year through 2037; meanwhile, operations at FAA and contract towers are forecast to increase 0.8% a year for the next 20 years with commercial activities growing at five times the rate of noncommercial activities (United States Federal Aviation Administration, 2017).

To reduce the environmental impact that traditional aviation engines cause, alternative aircraft propulsion solutions such as electric and hybrid aircraft have been a popular research topic. As the core part of the propulsive system of electric and hybrid aircraft, an electric motor uses electricity as an energy source instead of fuel.

Therefore, compared to conventional fuel-burning aviation engines, electric motors have zero emissions during flight and are generally quieter at the same power setting.

The automotive industry is ahead of aviation in applying electricity as a source of propulsion. Although similarities exist between the two industries, differences such as operation temperature ranges, weight limitations, and safety requirements make it necessary to study the aviation propulsive battery system design space separately.

Lithium-ion (Li-ion) batteries are frequently chosen as a propulsive electric source by ground electric vehicles and electric/hybrid aircraft. This is because of lithium-ion batteries' relatively high gravimetric specific energy, high efficiency, long calender and cycle lifetime, and low self-discharge (Stroe, Swierczynski, Kr, & Teodorescu, 2016). However, it should be noted that, although Li-ion batteries' gravimetric specific energy is the highest among all available types of batteries, it is still much lower than conventional aviation fuels (aviation gasoline and jet fuel). For example, the NCR18650GA lithium-ion battery's gravimetric specific energy is only 2.1% of AV-GAS 100LL (Shell, 1999) (Panasonic, 2017); and only 2.2% of Jet A (kerosene) fuel (Chevron Products Company, 2007).

Although Li-ion batteries have outstanding performance compared to most other batteries, they should only be used within manufacturer specified limits. Inaccurate state-of-charge and state-of-health estimations of Li-ion batteries can lead to complications such as over-current, over-voltage, or under-voltage, which can compromise the battery performance, shorten battery life, or cause catastrophic safety consequences.

The Eagle Flight Research Center (EFRC) under the Embry-Riddle Aeronautical University (ERAU) is one of the leading institutes of electric and hybrid aircraft research. The EFRC has been researching both hybrid and fully electric airplanes since 2011. One of its hybrid aircraft projects, Eco-Eagle, designed a parallel hybrid aircraft to achieve the goal of flying 200 passenger miles per gallon (PMPG) of fuel at an average speed of 100 miles per hour. It is designed to take-off using gasoline and then switch to electric power at cruising conditions. This project has participated in the Green Flight Challenge which was sponsored by Google and hosted by the National Aeronautics and Space Administration (NASA). Another project from EFRC modifies a Diamond HK-36 motor glider into a fully electric airplane that uses a lithium-ion battery pack to power a 100 HP electric motor. Its goal is to design and build the first fully electric airplane certifiable by FAA in the United States. At the same time, EFRC is also leading a hybrid electric research consortium that consists of world-leading aviation companies and organizations to investigate specific hybrid electric design tasks.

1.2   Problem Statement

The development of electric and hybrid airplanes has received increasing interest from the aviation industry. Due to the nature of aircraft weight sensitivity, lithium-ion batteries with high specific energy are frequently chosen as the propulsive energy carriers for electric and hybrid airplanes. Use of lithium-ion batteries for propulsion requires the development of a lightweight yet accurate in-flight energy estimation method that takes into account the battery health degradation. This thesis proposes an in-flight state-of-charge and state-of-health estimation algorithm that will serve as a battery "fuel gauge". It will adaptively estimate the instantaneous internal parameters of battery cells and further interpolate them to estimate the remaining energy of the propulsive battery pack. To validate this algorithm, a lithium-ion cell simulation model will be developed to simulate the cell behavior. Finally, the weight fraction of propulsive battery systems will be analyzed empirically.

1.3   HK-36 Electric Airplane

The HK-36 electric airplane "e-Spirit of St. Louis" project (referred to by HK-36 for the rest of the thesis) is one of the projects in Eagle Flight Research Center (EFRC). The project's goal is to modify the Diamond HK-36 motor glider into a fully electric airplane and to certify it with the FAA. The HK-36 is a starting point of this thesis. Some specific examples made in this thesis, as well as the weight analysis,

are based on the HK-36 propulsive battery system design. However, results and conclusions from this research will be generic and may be applied to any configuration of battery packs.

The original HK-36 airframe comes with a Rotax 914 engine to power a constant-speed three-blade propeller. This engine delivers a maximum continuous power of 100HP (75kW) (Diamond Aircraft, 1997). The modified HK-36 electric airplane replaces the Rotax engine with a YASA 750 axial flux electric motor that delivers the same maximum continuous power of 100HP (75kW) (YASA Motors, 2017). The original airplane stores its on-board energy source (100LL fuel) in a fuel tank; whereas in the electric airplane, a propulsive battery pack takes place of the fuel tank and carries the electricity energy to power the YASA motor.

The HK-36 propulsive battery pack contains a total of 2520 Li-ion cells. These cells are electrically connected in parallel and series to meet the power requirements of the motor. Figure 1.1 illustrates the configuration of the HK-36 propulsive battery pack. In this figure, each red rectangle represents one battery cell. Seven cells are connected in parallel to form a "cell unit." This is the lowest observability for the battery pack since only its combined current and terminal voltage can be observed by the battery management system (BMS). Then, 12 "cell units" are connected in series to form a "battery module", which is represented by the black rectangles in the diagram (also see Figure 1.2). Lastly, 30 of such "battery modules" are connected in parallel and series to form the entire battery pack.
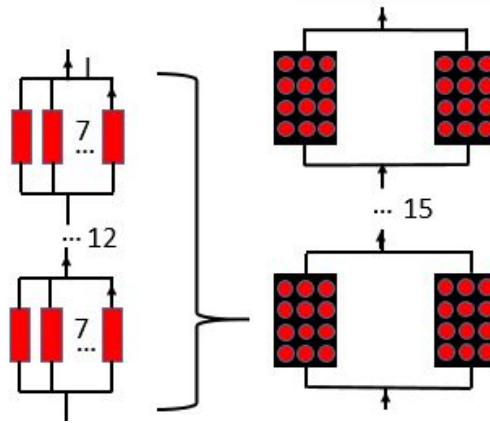
Figure 1.1 HK-36 Propulsive Battery Pack Configuration.
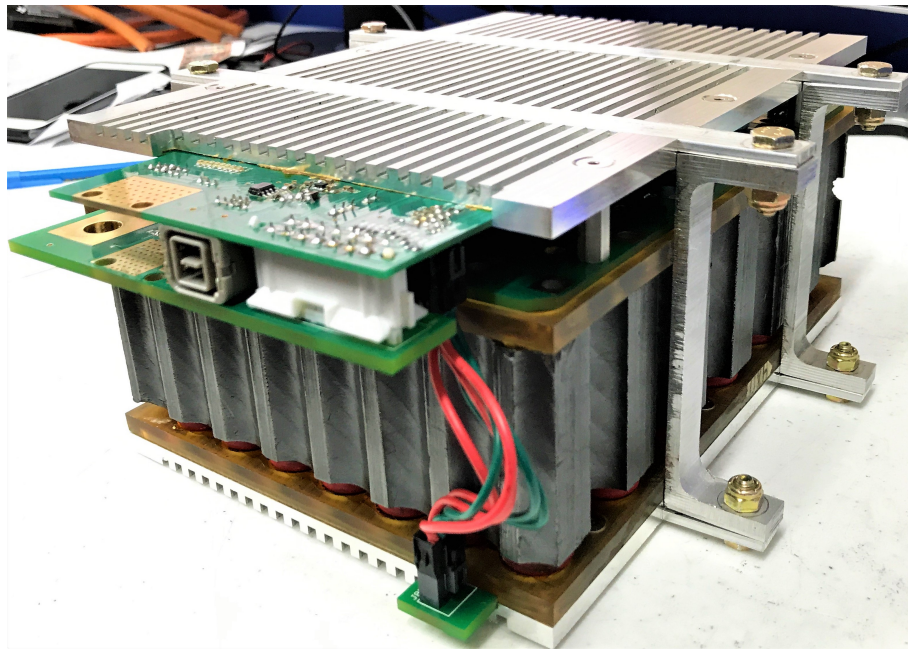
Figure 1.2 One Battery Module from the HK-36 Propulsive Battery Pack.

1.4   Propulsive Battery Systems

The most fundamental unit of a propulsive battery system is one single cell. The type of Li-ion cells that HK-36 uses is NCR18650GA manufactured by Sanyo under Panasonic (see Figure 1.3).

Figure 1.3 Panasonic-Sanyo NCR18650GA Single Cell.

"NCR" is a Panasonic short term for "Nickel/Cobalt/Rechargeable", which refers to the chemicals contained in the battery cells (Battery Bro, 2014). "18650" stands for the standard cylindrical size of the cells: 18 mm diameter of cross-section and 65 mm of height. Table 1.1 summarizes some key specifications of the NCR18650GA cells.

Table 1.1 Specifications of a NCR18650GA Cell

Items	Values
Weight	48 g (0.106 lb)
Typical capacity at 25ºC	3450 mAh
Nominal voltage	3.6 V

Based on these listed specifications, the NCR18650GA cells' specific energy can be calculated by Equation 1.1.

$$\epsilon_{Bat} = \frac{3.45Ah * 3.6V}{0.048kg} = 259 \text{ W-hr/kg} = 0.16 \text{ HP-hr/lb} \qquad (1.1)$$

Although Li-ion batteries have relatively higher specific energy than other types of batteries, the power and capacity that one single cell can deliver is limited and far from sufficient to power an electric motor or to complete a flight. Therefore, cells are usually connected in parallel, series, or a mixture of both to deliver desired power and capacity. When assembling battery cells into a pack, other components are required to assist the battery packs in delivering the electricity efficiently and safely. Battery cells, together with other auxiliary components, form a propulsive battery system.

A typical propulsive battery system consists of five sub-systems:

- Battery cells: store electricity;

- Housing structures: secure cells and other components in place during movement and vibration;

- Cooling system: passively or actively control the temperature of a battery pack;

- Battery management system (BMS): manage all of the cells within a battery pack and protect them from operating outside of the manufacturer specified limits;

- Wiring: electrically connect battery modules and deliver electricity to the motor.

1.5   Battery Packs in Aviation Application

An aviation propulsive battery system has numerous differences from a conventional fuel-burning system. Pilots who are switching from a traditional airplane to an electric airplane need to understand the differences before they take-off.

One of the differences a pilot might face first when preparing flight plans is that the weight of a propulsive battery system does not change during flight, which means that the landing weight remains almost the same as the take-off weight. In contrast, the weight of a fuel-burning propulsion system gradually decreases when the engine is consuming fuel.

Another difference is that the maximum power a battery pack can deliver will decrease during flight. Maximum deliverable power is distributed by maximum allowable current and terminal voltage from the pack. However, due to the nature of Li-ion batteries, their terminal voltages gradually decrease during discharge. As a result, the maximum deliverable power will decrease. For example, one NCR18650GA single cell's maximum allowable current is 8A; its terminal voltage will decrease from 4.2V to 2.5V during discharge. At the beginning of discharge, the theoretical maximum power it can deliver is 8A x 4.2V, while at the end of discharge, its maximum deliverable power reduces to 8A x 2.5V. Depending on the size (capacity) of a battery pack, it might not be able to deliver the same take-off power again after the initial take-off, even though the battery pack still has enough capacity left for cruising.

Moreover, unlike traditional fuel-burning airplanes whose fuel tank capacities remain constant, a Li-ion battery pack's capacity declines after each flight cycle. This is because of internal electrolyte loss of the battery cells during charging and discharging.

Not only are there differences between traditional aviation fuel-burning propulsion systems and propulsive Li-ion battery systems, but propulsive battery packs applied in aviation industry also differ from the ones in ground electrical vehicles (EVs) in the aspects of temperature range, safety, and weight.

Battery packs in electric airplanes operate in a wider temperature range than in ground EVs. When parked or taxiing, electric airplanes deal with the same ground temperatures as EVs. However, air temperatures at altitude are normally lower than on the ground. Battery packs in cruising electric airplanes are therefore exposed to lower ambient temperatures than in ground EVs.

Safety requirements of aviation battery packs are more restrictive than ground EVs. In dangerous situations, ground vehicles may brake and stop in relatively shorter time, while airplanes need comparatively longer time to descend and find open fields to land. This results in higher safety expectations for aviation battery packs.

Due to airplanes' sensitivity to weight and balance, aviation battery packs face more critical weight limitations than ground EVs. As a result, all of the auxiliary components inside of an aviation battery pack (such as BMS, wiring, cooling system, etc.) need to be lightweight.

2. Literature Review

2.1 Li-ion Single Cell Equivalent Circuit Model (ECM)

The first step when analytically studying a Li-ion battery cell's performance is to look at its single cell equivalent circuit model (ECM). An ECM theoretically models the chemical reaction inside of a battery cell as a nonlinear dynamical system that can be mathematically described. More than one Li-ion ECMs were created by researchers to fit different applications. In 2011, H.He et al. studied five types of commonly used ECMs. The dynamic performances of the five ECMs were compared; furthermore, the accuracies of their model-based state-of-charge (SOC) estimations were evaluated (He et al., 2011).

Among the five ECMs studied and compared by this reference, two of them are found to be more suitable in EV applications due to their better dynamic simulation results. They are the Thevenin model and the DP model. Figures 2.1 and 2.2 show the schematic diagrams of the two models individually.
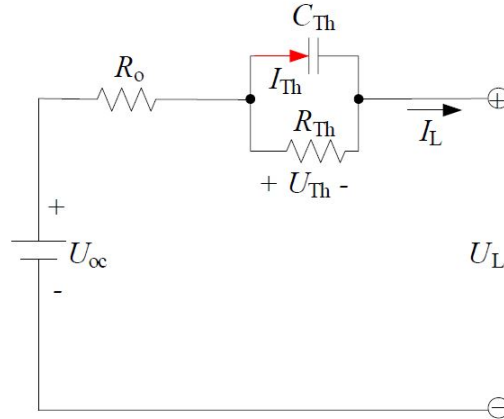
Figure 2.1 Schematic Diagram of the Thevenin Equivalent Circuit Model (He et al., 2011).
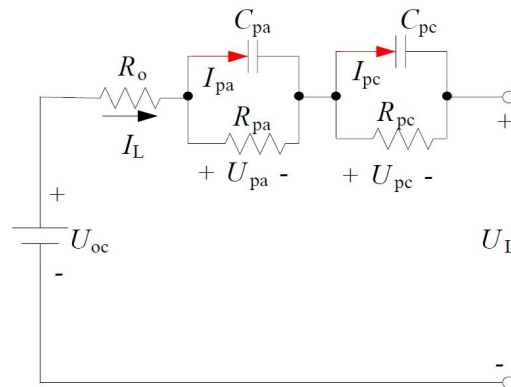
Figure 2.2 Schematic Diagram of the DP Equivalent Circuit Model (He et al., 2011).

The Thevenin model and the DP model schematic diagrams have similar structures, both being composed of three major parts:

- Open circuit voltage U_{OC}

- Ohmic resistance R_0

- RC parallel circuit(s) with a set of resistors R and capacitors C in each circuit

The DP model has one more RC parallel circuit than the Thevenin model. This is to refine the Li-ion cells polarization characteristics by simulating the concentration polarization and the electrochemical polarization separately. As a result, the DP model has better SOC estimation accuracy than the Thevenin model. Table 2.1 lists their absolute SOC estimation errors.

Table 2.1 Comparison of SOC Estimation Errors between the Thevenin model and the DP model (He et al., 2011).

Model	Maximum	Mean	Variance
Thevenin Model	0.0500	0.0101	0.0004
DP Model	0.0309	0.0047	0.00004

From Table 2.1, it is noteworthy that the SOC estimation mean error of the DP model almost doubles that of the Thevenin model; additionally, the DP model's error variance is 10 times less than the Thevenin model.

While the extra RC parallel circuit brings better SOC estimation accuracy, it also introduces one more differential equation to the model. Consequently, the DP model's SOC estimation rate will be slower than the Thevenin model, which only has one RC circuit (one differential equation). In other words, the estimation accuracy must trade-off with larger computational effort. Since the goal of this thesis is to achieve real-time SOC and SOH estimations, the algorithm's computational speed is as critical as its estimation accuracy. So, the Thevenin model is chosen as the equivalent circuit model for Li-ion cells in this thesis. It is also selected by a majority of

papers and articles for electric vehicles SOC and SOH estimation studies. However, everything done in this thesis for the Thevenin-based models can be replicated using DP models.

2.2   SOC Estimation Methods

Battery SOC is expressed in percentage to describe the energy left in a battery with respect to its available capacity (after considering health degradation). For example, a battery with 100% SOC is fully charged, while one with 0% SOC is empty. In an electric airplane, it functions like a fuel gauge on a conventional fuel-burning airplane. Unlike charging/discharging currents or terminal voltages, SOC is not a physical property of batteries that can be directly measured. In most situations, SOC is estimated by algorithms using other direct measurements.

Traditionally, two SOC estimation techniques are frequently used due to their simplicity. They are the coulomb counting method and open circuit voltage method, which will be introduced in the following two sub-sections.

2.2.1   Coulomb Counting Method

The Coulomb counting method is a rational way to estimate a battery's SOC. In this method, the current that is passing through the battery is monitored. Integrating the measured current over time gives an estimated energy loss (Chaoui, Golbon,

Hmouz, Souissi, & Tahar, 2015). Therefore, SOC can be defined with Equation 2.1, where E_{Bat} is the battery's available capacity.

$$\text{SOC} = \frac{E_{Bat} - \int I dt}{E_{Bat}} \tag{2.1}$$

The Coulomb counting method is simple, straightforward, and easily achieved on-line. However, one of its main drawbacks besides startup errors, is that, due to the integral, the measurement errors will accumulate over time, resulting in SOC estimation drift.

2.2.2 Open Circuit Voltage Method

Another conventional SOC estimation technique is the open circuit voltage (OCV) method. By definition, the open circuit voltage is the battery voltage under equilibrium conditions (Snihir, Rey, Verbitskiy, Belfadhel-Ayeb, & Notten, 2006). The OCV method uses the correlation between OCV and electrolyte concentration that varies with SOC. This correlation can be further represented by an OCV-SOC plot. This plot is expected to remain the same during the life-time of the battery, i.e. it does not depend on the age of the battery (Snihir et al., 2006). This makes OCV an excellent indicator of SOC. But even for the same type of battery, different cells do not have exactly the same OCV-SOC plots. However, they are close to each other with an acceptable error. Figure 2.3 shows the OCV-SOC relationships of 9 fresh batteries measured under the same conditions (Lee et al., 2008). From the figure, it can be seen that the absolute maximum differences among the nine batteries at the same

SOC are less than 0.05V when SOC is from 50% to 100% and less than 0.1V when SOC is 0-50%.
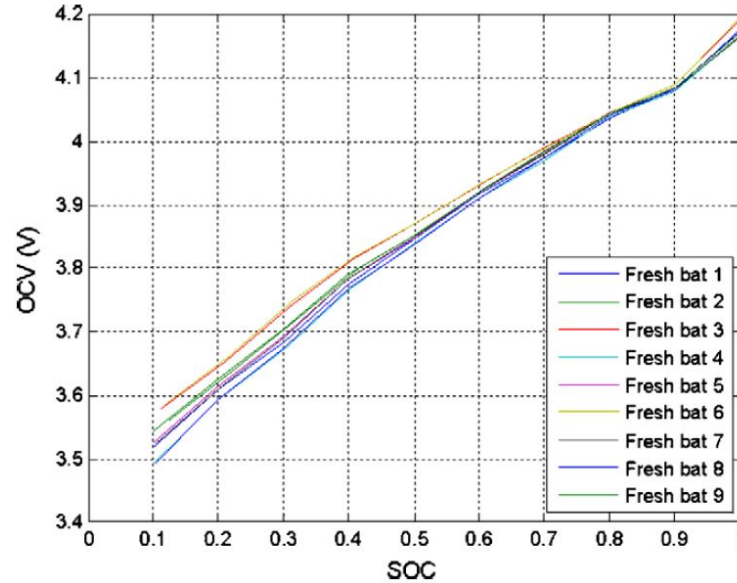
Figure 2.3 OCV-SOC Relations of Nine Batteries (Lee et al., 2008).

The OCV-SOC relation is also stable with variation of temperatures (Huria et al., 2012). This can be verified by Figure 2.4 , which shows the OCV-SOC plots obtained from the same Li-ion battery cell discharging under three different temperatures (5^oC, 20^oC and 40^oC).

Using the OCV method to estimate SOC is more accurate than the coulomb counting method. However, in order to measure a battery cell's OCV, the cell needs to be off-loaded for hours to reach the steady state (Chaoui et al., 2015). An on-line estimation algorithm obviously cannot use this method.
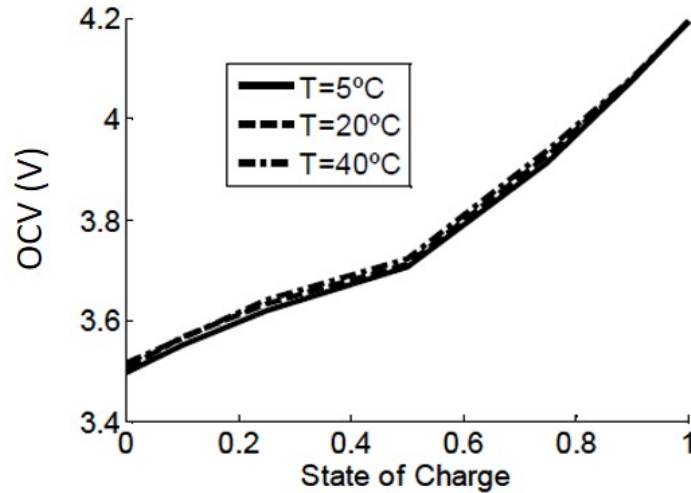
Figure 2.4 OCV-SOC Relations under Different Temperatures (Huria et al., 2012).

In this thesis, the OCV method will be revised to estimate SOC. Instead of directly measuring a battery's OCV at steady state, an algorithm will be utilized to estimate the OCV in real-time and further translate the OCV into SOC information.

2.3 SOH Estimation Methods

Li-ion batteries degrade as a result of their usage and exposure to environmental conditions. This degradation affects the cells' ability to store energy, meet power demands and ultimately leads to their end-of-life (EOL) (Birkl, Roberts, McTurk, Bruce, & Howey, 2017). Therefore, it is crucial for battery pack users to be certain of the state-of-health (SOH) of the batteries to avoid misusing the battery packs.

Similar to SOC, SOH is also expressed as a percentage. Depending on the applications, there are usually two indicators of SOH – battery internal impedance and

capacity (Huang & Qahouq, 2014). Based on these two indicators, multiple SOH estimation methods have been introduced.

One simple SOH estimation method uses the battery's capacity as an indicator. This method monitors the time needed for a fully charged battery to be completely discharged by a small constant load. Utilizing the coulomb counting method, the total energy loss can be calculated. The total energy loss is then equal to the battery's available capacity. However, it usually takes many hours to fully discharge a battery and get its available capacity. Moreover, this method cannot be used during the battery's operation (Chaoui et al., 2015).

Another SOH estimation method regards the battery's impedance as an indicator by using electrochemical impedance spectroscopy (EIS). This method injects a small sinusoidal voltage or current signal to an electrochemical cell, measuring the system's response with respect to amplitude and phase, determining the impedance of the system by complex division of AC voltage by AC current, and repeating this for a certain range of different frequencies (Karden, Buller, & Doncker, 2000). By analyzing the impedance spectrum obtained from EIS, one can get the estimated impedance of a battery. However, the EIS method requires additional hardware, costly measurement, analysis instrumentation, and interruption of the system's operation (Chaoui et al., 2015).

Comparing the actual impedance of a battery with a reference impedance value can be utilized as a measure of battery SOH as well. This reference impedance can

either be the impedance when the battery is new, or a value that is set based on long-term experimental data (Huang & Qahouq, 2014).

This thesis proposes a hybrid approach that combines the methods mentioned above to achieve on-line real-time SOH estimation.

2.4   Battery Pack Modeling

As discussed in the introductory chapter, multiple Li-ion cells need to be connected into a pack to deliver the desired power and capacity. This raises the demand to investigate battery pack modeling approaches. However, the majority of studies about Li-ion battery SOC and SOH estimations focus on the single cell model. Only a few of them discuss the pack model, such as the studies from Tripathy (2014) and Xiong (2013).

2.4.1   Cells Connected in Parallel

Tripathy researches cases where Li-ion cells are connected in parallel (Tripathy, McGordon, Marco, & Gama-Valdez, 2014). This research focuses on fault detection among parallel connected cells. Although fault detection is not the focus of this thesis, the article states that under normal operation, cells connected in parallel maintain identical voltages, which results in the pack self-balancing to match terminal voltage and SOC. This reference concludes that, if all cells are arranged in parallel, they can

be considered as a single "big" cell, with identical voltages and compounded capacities (Tripathy et al., 2014).

This thesis uses this idea. In the HK-36 example, the minimum observability is one "cell unit" – 7 cells connected in parallel – since no single cell within a cell unit can be observed by the BMS. In order to estimate their SOC and SOH, such a "cell unit" will be treated as a single "big" cell as Tripathy suggested in his paper.

2.4.2   Cells Connected in Series

In another article, Xiong analyzed the battery packs composed of Li-ion cells connected in series (Xiong et al., 2013). Unlike cells connected in parallel where self-balancing is done naturally, serial connected cells face the problem of capacity and resistance unbalancing. To overcome the cell-to-cell variations problem, the authors propose a cells filtering approach, where cells are pre-screened and only the ones with similar capacities and resistances are selected to be connected in series. Following the cells filtering process, the lumped parameter battery model with N cells is simplified as a single cell model. Figure 2.5 illustrates how the serial connected cells are simplified into a unit model.
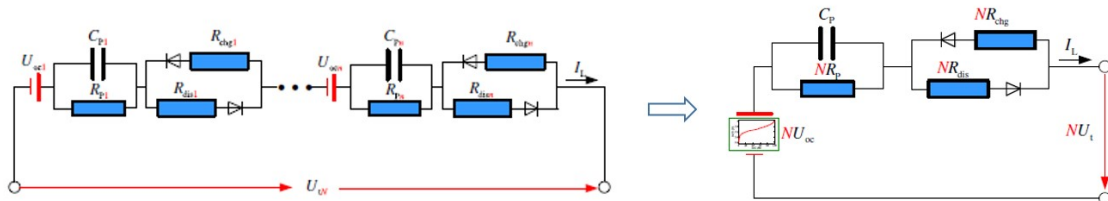
Figure 2.5 Simplify Serial Connected Cells into a Unit Model (Xiong et al., 2013).

But, in most of the real world applications (including the HK-36 example), the terminal voltage of each cell or "cell unit" in series is observed by the BMS. Thus there is no need to simplify serial connected cells into a unit model.

2.5   Parameter Estimation

Parameter estimation functions as a mathematical tool that estimates the system parameters by analyzing the system input or output information. Several common parameter estimation methods are available and two of the most often used are introduced in this section.

2.5.1   Regular Least Squares

Regular least squares estimation is one of the commonly chosen parameter estimation approaches. Regular least squares assumes that the system measurements (outputs) are corrupted with measurement errors, and the goal is to find a linear combination of system parameters that gives the best fit to the noisy data (Gibbs, 2011). The system can be described by Equation 2.2 (Balas, 2017).

$$\underline{y} = H * \underline{\theta} + \underline{\epsilon} \tag{2.2}$$

$\underline{y}$ – system measurements (outputs) vector

H – system excitation matrix

$\underline{\theta}$ – system parameters vector

$\underline{\epsilon}$ – system uncertainty (measurement error) vector

Expanding the vector terms, we get Equation 2.3 or Equation 2.4 (Balas, 2017).

$$\begin{bmatrix} y_1 \\ y_2 \\ \cdots \\ y_m \end{bmatrix} = \begin{bmatrix} \underline{h}_1 & \underline{h}_2 & \cdots & \underline{h}_N \end{bmatrix} \begin{bmatrix} \theta_1 \\ \theta_2 \\ \cdots \\ \theta_N \end{bmatrix} + \underline{\epsilon} \tag{2.3}$$

$$\underline{y} = \theta_1 \underline{h}_1 + \theta_2 \underline{h}_2 + \cdots + \theta_N \underline{h}_N + \underline{\epsilon} \tag{2.4}$$

When the system is described with a regression model, its estimated outputs at n^{th} time step can be expressed as Equation 2.5 (Balas, 2017).

$$\hat{\underline{y}}(n) = \sum_{i=1}^{M} \hat{\underline{\theta}}_i(n-1)\underline{h}(n-1) \tag{2.5}$$

$\hat{\underline{y}}(n)$ – estimated system measurements (outputs) vector at n^{th} time step;

$\hat{\underline{\theta}}(n-1)$ – unknown parameters vector at $(n-1)^{th}$ time step;

$\underline{h}(n-1)$ – system excitation at $(n-1)^{th}$ time step.

The estimated parameters can then be calculated by taking the orthogonal projection of the system measurements (Balas, 2017). Equation 2.6 shows the least squares estimator.

$$\hat{\underline{\Theta}}_{n-1} = (H_n^T H_n)^{-1} H_n \underline{Y}_n \tag{2.6}$$

Note that Equation 2.5 describes the system in each time step. To distinguish between Equations 2.5 and 2.6, Equation 2.6 uses capital letters for the three terms $(\Theta, H$ and $Y)$. Each capital letter represents a matrix that contains information from beginning to the current time step. For example, $\hat{\underline{y}}(n)$ is the estimated system measurement vector at n^{th} time step, whereas $\hat{\underline{Y}}_n$ is a matrix containing vectors from the beginning to the nth time step.

The regular least squares estimator works well in the cases where the system measurements Y and excitation matrix H can be obtained all at once. On the contrary, in on-line estimation tasks, the system measurements and excitation matrices can only be obtained sequentially from the sensors. Due to the high computational cost, it is very inefficient to repeat Equation 2.6 at each time step to calculate the parameters since the equation involves substantial matrix operations. Therefore, it is essential to have a faster parameter estimation method for on-line estimation tasks.

2.5.2 Recursive Least Squares

To solve the mentioned problem that the regular least squares estimator has, this section introduces an updated parameter estimation method – recursive least squares (RLS). The forgetting factor λ term is introduced in RLS. λ $(0 < \lambda \leq 1)$ is an exponential factor that is applied to each error term. Equations 2.7 and 2.8 compare the error terms between regular least squares and RLS.

In regular least squares, the error ϵ is expressed as Equation 2.7.

$$\epsilon(n) = \sum_{i=0}^{n} e^2(i) \tag{2.7}$$

In RLS, the error is modified as Equation 2.8 (Rowell, 2008).

$$\epsilon(n) = \sum_{i=0}^{n} \lambda^{n-i} e^2(i) \tag{2.8}$$

The purpose of λ is to weigh recent data points most heavily, and thus track changing statistics in the input data (Rowell, 2008). For example, in Equation 2.8, when $i = n$ (newest input data), the exponential term λ^{n-i} equals 1, and hence the error term $e^2(n)$ is the most heavily weighed in the sum; conversely, when $i = 0$ (oldest input data), term λ^{n-i} equals $\lambda^n \leq 1$, and therefore the error term $e^2(0)$ is the most lightly weighed in the sum.

The advantage of RLS over regular least squares is that instead of re-estimating the parameters using Equation 2.6 every time step when the system receives new input data, RLS is able to apply an iterative algebraic procedure to update the parameters using the results from previous time step, thus saving significant computational effort (Rowell, 2008).

RLS has also been proven to be asymptotically stable and the parameters are exponentially convergent provided that the system input is persistently exciting (Johnstone, Johnson, Bitmead, & Anderson, 1982). Equation 2.9 shows the convergence of RLS estimator error $\epsilon(n)$ (Balas, 2017).

$$||\epsilon(n)|| \leq K_0 \lambda^n ||\epsilon(0)|| \tag{2.9}$$

3. Methodology

3.1   Li-ion Battery Equivalent Circuit Model (ECM)

Recall that in the literature review chapter, the Thevenin model is selected as the Li-ion battery equivalent circuit model for this thesis. Figure 3.1 (modified from Figure 2.1) illustrates the schematic diagram of Thevenin model.
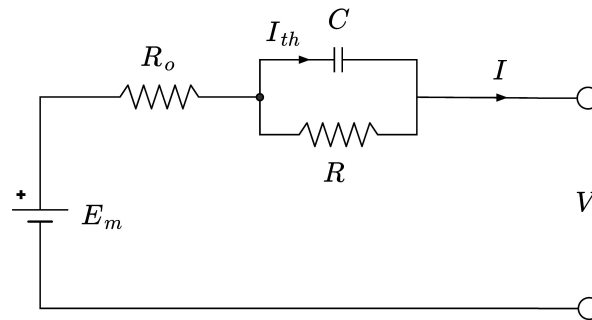
Figure 3.1 Schematic Diagram of the Thevenin Equivalent Circuit Model.

The Thevenin Model consists of three parts:

- Open circuit voltage E_m

- Ohmic resistance R_0

- One RC parallel circuit with resistor R and capacitor C

In this model, the parameters of interest are E_m, R_0, R, and C. With these four parameters, the system can be described by Equation set 3.1 with a first order differential equation and a linear equation.

$$\begin{cases} \dot{V}_{RC} = -\frac{1}{RC}V_{RC} + \frac{1}{C}I \\ V = E_m - V_{RC} - R_0 I \end{cases} \tag{3.1}$$

where:

I – Current

V – Terminal voltage

V_{RC} – Voltage across RC parallel circuit

In order to estimate the parameters of interest, the first step is to transform the system equations into a regression model. Equations 3.2 through 3.7 show the transformation process:

Re-organize the second line in Equation set 3.1 to get V_{RC}:

$$V_{RC} = E_m - V - R_0 I \tag{3.2}$$

Take derivatives of both sides from Equation 3.2:

$$\dot{V}_{RC} = -R_0 \dot{I} - \dot{V} \tag{3.3}$$

It is reasonable to assume that E_m and R_0 are slowly time-varying, so that $\dot{E}_m \approx 0$ & $\dot{R}_0 \approx 0$.

Next, substitute V_{RC} and $\dot{V}_{RC}$ back into the first line in Equation set 3.1:

$$-R_0 \dot{I} - \dot{V} = -\frac{1}{RC}(E_m - R_0 I - V) + \frac{1}{C}I \tag{3.4}$$

Multiply both sides of Equation 3.4 by RC:

$$-RCR_0\dot{I} - RC\dot{V} = -E_m + R_0 I + V + RI \qquad (3.5)$$

Solve for V:

$$V = E_m - RC\dot{V} - RCR_0\dot{I} - (R + R_0)I \qquad (3.6)$$

At last, the regression model of Thevenin Li-ion battery equivalent circuit model can be recovered from Equation 3.6:

$$V = \begin{bmatrix} 1 & \dot{V} & \dot{I} & I \end{bmatrix} \begin{bmatrix} E_m \\ -RC \\ -RCR_0 \\ -(R + R_0) \end{bmatrix} \qquad (3.7)$$

3.2 Recursive Least Squares (RLS)

After obtaining the Li-ion single cell equivalent circuit model's regression model, the next step is to apply the RLS estimator to it. Equations 3.8 through 3.11 respectively illustrate the $y(n)$, $\underline{f}(n)$, and $\underline{b}(n-1)$ with the corresponding terms from the regression model.

$$y(n) = \underline{f}^T(n)\underline{b}(n-1) \qquad (3.8)$$

$y(n)$ – system measurements (terminal voltage $V(n)$) at n^{th} time step:

$$y(n) = V(n) \qquad (3.9)$$

$\underline{f}^T(n)$ – system excitation vector (or RLS system input information) at n^{th} time step:

$$\underline{f}^T(n) = \begin{bmatrix} 1 & \dot{V}(n) & \dot{I}(n) & I(n) \end{bmatrix} \qquad (3.10)$$

$\underline{b}(n-1)$ – estimated parameters vector at $(n-1)^{th}$ time step:

$$\underline{b}(n-1) = \begin{bmatrix} E_m(n-1) \\[6pt] -R(n-1)C(n-1) \\[6pt] -R(n-1)C(n-1)R_0(n-1) \\[6pt] -[R(n-1) + R_0(n-1)] \end{bmatrix} \qquad (3.11)$$

As discussed in the literature review chapter, RLS algorithm does not re-compute Equation 2.6 at each time step; instead, it updates the estimated parameters with an iterative algebraic process using information from the previous time step. The iterative process is illustrated in the flow chart in Figure 3.2.
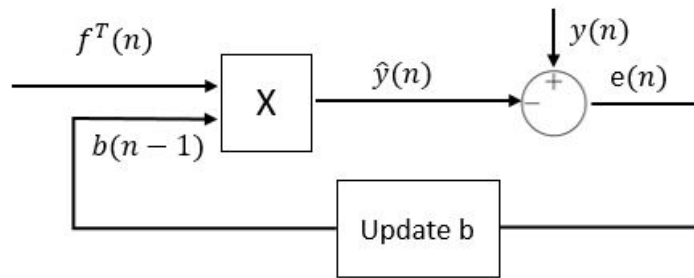
Figure 3.2 RLS Iterative Process Algorithm.

The iterative process can also be described mathematically by Equations 3.12 through 3.16 (Rowell, 2008).

Estimate the current system output with the system excitation from the current time step and estimated parameter vector from the previous time step:

$$\hat{y}(n) = \underline{f}^T(n)\underline{b}(n-1) \tag{3.12}$$

Calculate the current error by comparing the current estimated system output with the current measured output:

$$e(n) = y(n) - \hat{y}(n) \tag{3.13}$$

Update $\underline{k}(n)$:

$$\underline{k}(n) = \frac{R^{-1}(n-1)\underline{f}(n)}{\lambda + \underline{f}^T(n)R^{-1}(n-1)\underline{f}(n)} \tag{3.14}$$

Update $R^{-1}(n)$:

$$R^{-1}(n) = \lambda^{-1}[R^{-1}(n-1) - \underline{k}(n)\underline{f}^T(n)R^{-1}(n-1)] \tag{3.15}$$

Update parameter vector b(n):

$$\underline{b}(n) = \underline{b}(n-1) + \underline{k}(n)e(n) \tag{3.16}$$

Detailed derivations of the above equations and explanation about k(n) and $R^{-1}(n)$ can be seen in MIT online course notes "Introduction to Recursive-Least-Squares (RLS) Adaptive Filters" written by D. Rowell (Rowell, 2008).

3.3   SOC and SOH Estimations

With an RLS estimator, the system parameters vector $\underline{b}(n)$ can be estimated in real-time. However, $\underline{b}(n)$ does not explicitly give any SOC or SOH information. This section proposes SOC and SOH estimation approaches using estimated $\underline{b}(n)$ information.

The estimated parameter vector $\underline{b}(n)$ takes the form:

$$\underline{b}(n) = \begin{bmatrix} b_1 \\ b_2 \\ b_3 \\ b_4 \end{bmatrix} = \begin{bmatrix} E_m \\ -RC \\ -RCR_0 \\ -(R+R_0) \end{bmatrix} \tag{3.17}$$

Although Equation 3.17 does not directly give the four parameters of interest individually (E_m, R_0, R, and C), they can be easily calculated from the four terms in $\underline{b}(n)$. The results are shown in Equation set 3.18 below:

$$\begin{cases} E_m = b_1 \\ R_0 = b_3/b_2 \\ R = -b_4 - b_3/b_2 \\ C = \frac{b_2^2}{b_2 b_4 + b_3} \end{cases} \tag{3.18}$$

Once the four parameters of interest are calculated from $\underline{b}(n)$, the SOC and SOH information can be estimated by the approaches in the next two sub-sections.

3.3.1 SOC Estimation

As mentioned in Section 2.2, this thesis revises the OCV method for SOC estimation. Instead of directly measuring the OCV of a battery after waiting hours for it to reach the steady state, the RLS algorithm allows OCV information ($E_m = b_1$) to be estimated on-line in real-time. Thus, the SOC can be estimated through the OCV-SOC look-up-table.

The OCV-SOC look-up-table will be obtained from the Design Optimization Tool embedded in Simulink®. The Design Optimization Tool is a parameter estimation tool that fits the single cell simulation model (discussed in Section 3.5) to the battery experimental data. Since it is just a tool that helps estimate parameters and collect OCV-SOC look-up-tables, details of applying this tool can be seen in the article from Huria (2012) and will not be reviewed in this thesis (Huria et al., 2012).

3.3.2 SOH Estimation

Section 2.3 reviewed literatures that study Li-ion battery SOH estimation methods. From those literatures, it can be found that both a battery's capacity and impedance (Z) can be used as indicators of SOH. This thesis uses a combination of both indicators by assuming that both capacity and impedance have linear relations with SOH. In other words, Z-SOH and SOH-Capacity relations can be described by linear look-up-tables. First, by knowing a battery's impedance Z, the Z-SOH look-up-table is used to estimate SOH (discussed further in this section). Then, the

SOH-Capacity look-up-table is used to evaluate the actual capacity of a battery (discussed further in Section 3.3.3). SOH serves as an intermediate parameter to correlate the estimated Z with capacity.

Before talking about a battery's state-of-health (SOH), a definition of "health" needs to be given. The battery industry usually uses a term called end-of-life (EOL), which is a customizable threshold that denotes when the battery is not usable anymore. Depending on different applications, EOL could be defined accordingly. For example, one of the common definitions of EOL is "once the battery resistance (impedance) increases to 160% of its initial value at the same condition" (Chaoui et al., 2015) (Gholizadeh & Salmasi, 2014). In this thesis, the definition of EOL is customized as follows:

> The capacity of a cell decreases to 60% of its initial capacity (about 500 cycles) at the same conditions (same temperature and same SOC); Meanwhile, the impedance of a cell increases to 160% of its initial impedance at the same conditions.

Figure 3.3 visualizes the definition of EOL. This figure is modified from the Capacity-Cycle plot obtained from the official datasheet of NCR18650GA cells from Panasonic.

The SOH can then be expressed as a percentage and it is defined by the linear Equation 3.19:

$$\text{SOH} = \frac{Z_{EOL} - Z_{act}}{Z_{EOL} - Z_0} * 100\% \tag{3.19}$$
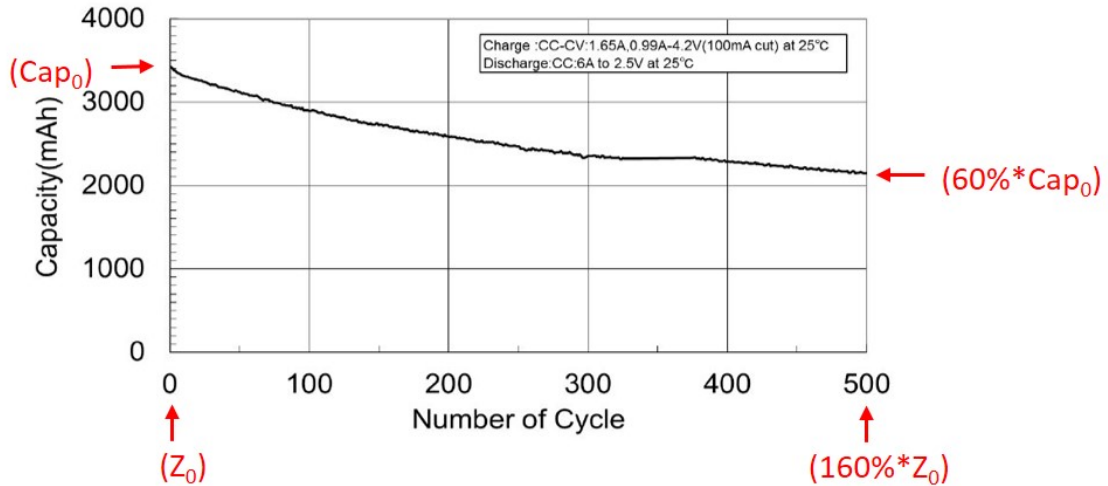
Figure 3.3 Capacity-Cycle Relation of a NCR18650GA Battery Cell (Panasonic, 2017).

where:

Z_{act} – Battery actual impedance

Z_0 – Battery initial impedance (when the battery has 0 cycle)

Z_{EOL} – Battery end-of-life impedance (assume $Z_{EOL} = 160\% * Z_0$)

In order to further analyze a Li-ion battery's impedance, a mathematical model of impedance Z must be derived from the battery equivalent circuit model. Equations 3.20 through 3.25 illustrate the derivation process of a Li-ion battery's impedance based on the Thevenin ECM.

To start, a few assumptions need to be made to make the derivation process possible:

- Current I is constant over each time step

- Initial time $t_0 = 0$

- Initial voltage across the RC parallel circuit $V_{RC}(0) = 0$

The derivation process starts with the system of equations, which is repeated in Equation set 3.20:

$$\begin{cases} \dot{V}_{RC} = -\frac{1}{RC}V_{RC} + \frac{1}{C}I \\ V = E_m - V_{RC} - R_0 I \end{cases} \tag{3.20}$$

Solve the first order differential equation in Equation set 3.20 for term V_{RC}:

$$V_{RC} = e^{-\frac{1}{RC}t}V_{RC}(0) + RI(1 - e^{-\frac{1}{RC}t}) \tag{3.21}$$

Since it is assumed that $V_{RC}(0) = 0$, the first term in Equation 3.21 can be dropped. Therefore, V_{RC} can then be expressed as Equation 3.22

$$V_{RC} = RI(1 - e^{-\frac{1}{RC}t}) \tag{3.22}$$

Substitute Equation 3.22 back into the second line in Equation set 3.20 and write out the terminal voltage V:

$$V = E_m - [R(1 - e^{-\frac{1}{RC}t}) + R_0] * I \tag{3.23}$$

The battery impedance can be extracted from Equation 3.23

$$Z = \frac{E_m - V}{I} = R(1 - e^{-\frac{1}{RC}t}) + R_0 \tag{3.24}$$

The equivalent impedance Z of a Li-ion single cell is:

$$Z = R(1 - e^{-\frac{1}{RC}t}) + R_0 \tag{3.25}$$

It can be seen that by Equation 3.25, a Li-ion single cell's impedance Z can be calculated with the R and R_0 information estimated from RLS.

The impedance, Z, obtained here is the battery's actual impedance, Z_{act}. To get its SOH, the initial impedance of a brand new battery Z_0 is also needed. Consequently, the initial R and R_0 information is needed, which will also be obtained by the Simulink® Design Optimization Tool with experimental data from brand new batteries.

3.3.3 Remaining Energy Estimation

SOC and SOH information is important for a battery. However, the ultimate goal for a battery SOC and SOH estimation algorithm is to display a battery's remaining energy directly. In another words, instead of SOC and SOH values, a battery "fuel gauge" is in demand for pilots.

The original chart in Figure 3.3 is obtained from the Panasonic NCR18650GA official datasheet, which summarizes the experimental data showing how battery capacity changes after numbers of cycles. A cycle means that a battery experiences a full charge followed by a full discharge. The data in the chart is only valid when the battery is always charged and discharged with the same current profile as indicated on the chart. However, users do not necessarily charge or discharge the battery packs

completely every time, nor do they use the same charge/discharge current as indicated on the chart. This makes it difficult to keep track of or quantify the number of cycles used. Therefore, the capacity-cycles relation in Figure 3.3 can not be directly applied for capacity estimation. Instead, SOH can be used as an intermediate parameter to correlate the impedance with capacity.

By assuming that SOH has a linear relation with number of cycles, the x-axis (number of cycle) in Figure 3.4 can be replaced with SOH. Therefore, the Capacity-Cycle chart can be transformed into a Capacity-SOH chart.
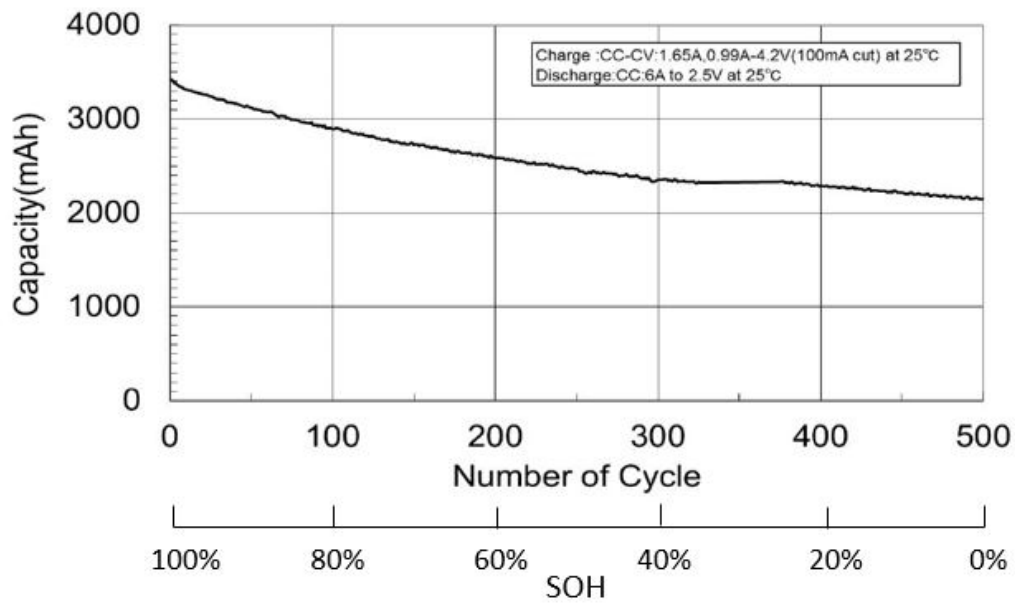

Figure 3.4 Capacity-Cycle Relation of a NCR18650GA Battery Cell with Modified Horizontal Axis (Panasonic, 2017).

Section 3.3.2 has explained how to get SOH from the estimated parameters (R and R_0). Now with SOH, the battery's actual capacity can be obtained through the Capacity-SOH chart.

The battery's remaining energy then can be expressed in Equation 3.26.

$$e_{remain} = e_{Bat} * \text{SOC} \tag{3.26}$$

e_{remain} – A battery cell's remaining energy

e_{Bat} – A battery cell's actual capacity

3.4   Pack Modeling

The SOC, SOH, and the remaining energy estimation algorithms previously discussed are all for a Li-ion single cell. However, in real cases, Li-ion cells are usually assembled into a battery pack. Therefore, it is also important to study the SOC, SOH, and the remaining energy estimation methods for battery pack applications.

Figure 3.5 illustrates an example battery pack model with two "cell units" connected in series. Each cell unit contains n cells connected in parallel.

Usually, in a battery pack like this, the main-string current I and the terminal voltages V_n are monitored by the BMS.

As discussed in Section 2.4.1, the n cells connected in parallel are assumed to be identical. Therefore, each cell receives equivalently split current $\frac{I}{n}$. By inputing the terminal voltage V and split current $\frac{I}{n}$ into the single cell RLS algorithm, the remaining energy of a single cell can be estimated. Also, since the n cells connected in parallel are identical, their compounded remaining energy E_{remain} will be n times the single cell remaining energy e_{remain}. This approach can be described by the flow chart in Figure 3.6.
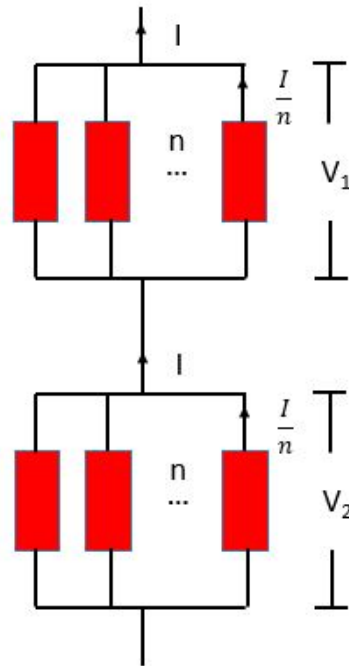
Figure 3.5 Example Battery Pack Configuration.
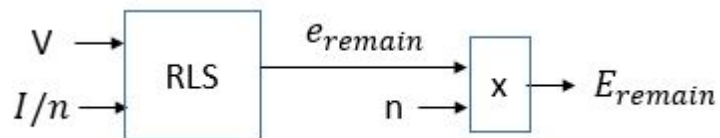

Figure 3.6 Battery Packs Remaining Energy Estimation Algorithm.

The E_{remain} obtained is the total remaining energy for one "cell unit". Different E_{remain}'s for different "cell units" will be estimated by each RLS correspondingly since each individual "cell unit" is observable by BMS. The BMS will also provide a balancing function to solve the imbalances among all E_{remain}'s.

3.5 Single Cell Simulation Model

In order to effectively validate the RLS algorithm's estimation accuracy, experimental data from real Li-ion battery cells being discharged under different conditions must be obtained. However, extensive equipment and software are required to set up experiments under different discharging conditions (such as different ambient temperatures and load currents). Additionally, it is very difficult to control or monitor the internal parameters of a Li-ion cell during discharging. Moreover, it is time-consuming to repeat the experiments since each charging and discharging cycle can take hours to finish. Due to these difficulties, a Li-ion single cell simulation model that is able to accurately simulate real cell performances is very beneficial.

One such model was developed by MathWorks®, Inc. using the Simscape® language. The original model was designed to simulate multi-temperature Li-ion battery performance with thermal dependence. This model essentially transforms a Thevenin equivalent circuit model into a Simulink® model. The internal parameter look-up-tables in this model are estimated by the Simulink® Design Optimization Tool using pulse current discharge tests on high power lithium cells (LiNi-CoMnO2 cathode and graphite-based anode) under different operating conditions. The model was validated for a lithium cell with an independent drive cycle resulting in voltage accuracy within 2% (Huria et al., 2012).

This thesis, however, modifies the single cell simulation model to fit the needs of this research. The major modification is that the internal parameter look-up-tables

in this model are estimated by the Design Optimization Tool using modified pulse current discharge profiles on NCR18650GA Li-ion cells. The thermal effect is not included in this model. All experimental data used for this modified model are evaluated at 25^oC ambient temperature. Figure 3.7 shows the core of the modified single cell simulation model.
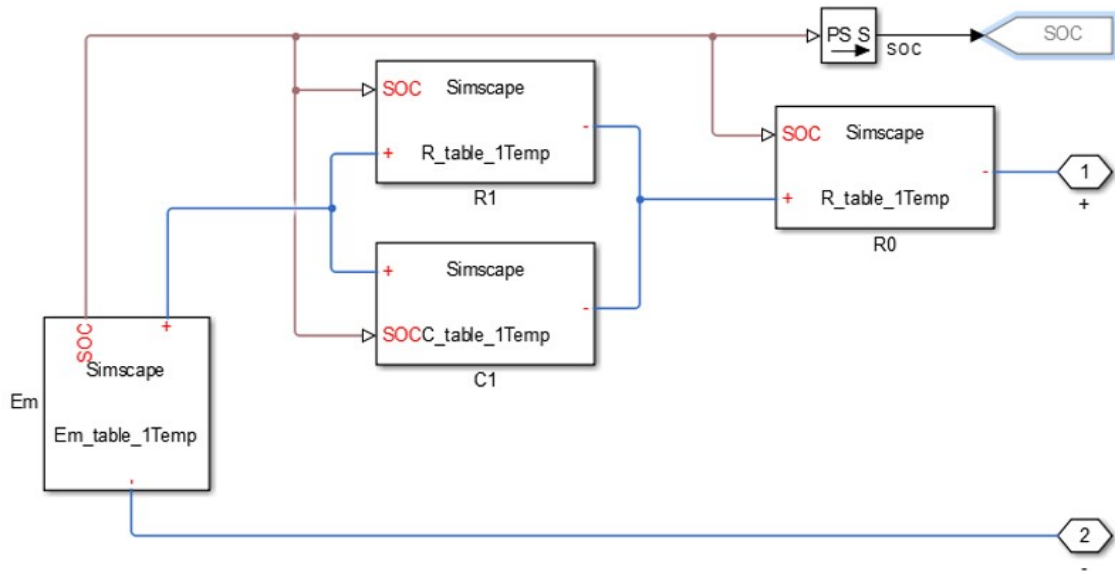

Figure 3.7 Li-ion Single Cell Simulation Model.

3.6 Weight Analysis

In the aviation industry, weight and balance are two of the most sensitive design factors, since nearly all of the aircraft performance has direct or indirect relation with the aircraft gross weight.

The aircraft maximum gross take-off weight (MGTOW), W_0, can be broken down into the weight of each individual system that makes up the entire aircraft. Each system can be further broken down into multiple sub-systems. To optimize each system or sub-system's performance while not compromising the aircraft MGTOW, it is necessary to analyze the ratio of the weight of a certain sub-system to another higher level system. Such a ratio is named as each system or sub-systems weight fraction, w. For example, w_{Bat} represents the weight fraction of the battery system; w_{Motor} represents the weight fraction of the motor system, etc.

The propulsive battery system for electric airplanes functions as the fuel system to the conventional fuel-burning aircraft. Its system weight, W_{Bat}, and corresponding weight fraction, w_{Bat}, are of great interest to electric aircraft designers.

In the example of the HK-36 electric airplane, its propulsive battery system weight consists of five parts: total weight of Li-ion cells W_{Cell}, weight of housing structures W_{House}, weight of its cooling system W_{Cool}, weight of the battery management system W_{BMS}, and weight of the harness wiring system W_{Wire}. Equation 3.27 mathematically describes the idea of their weight fractions.

$$w_{Bat} = \frac{W_{Bat}}{W_0} = \frac{W_{Cell} + W_{House} + W_{Cool} + W_{BMS} + W_{Wire}}{W_0} * 100\% \qquad (3.27)$$

This thesis focuses on empirically analyzing the weight of a propulsive battery system and its sub-systems as well as their weight fractions. All weight analysis will be based on the propulsive battery system designing experiences from the HK-36 electric airplane project. For each sub-system that makes up the HK-36 propulsive battery system, two types of weight fractions will be studied: One is the weight fraction of each sub-system in relation to the aircraft MGTOW, W_0; the other is the weight fraction of each sub-system in relation to the propulsive battery system total weight, W_{Bat}. Finally, analysis of how specific energy variances and stored energy differences affect the weight fractions of each sub-system within the propulsive battery system will be performed.

4. Results and Analysis

4.1 Single Cell Parameter Estimation

The equipment used to collect NCR18650GA battery cells' experimental test data is the Vencon UBA5 Battery Analyzer & Charger. The UBA5 has two channels. Each channel connects to the positive and negative terminals of one tested cell. At the same time, the UBA5 is also connected to the computer with an RS232 cable. Figure 4.1 illustrates the experiments setup for single cell testings.

Figure 4.1 Single Cell Test Setup with the Vencon UBA5 Battery Analyzer & Charger.

The discharging current profile for the NCR18650GA single cell tests is 3.3A (1C) pulses for 6 minutes, each followed by an one-hour rest (no current) to reach steady state open circuit voltage (OCV). Both the input discharging currents and the responsive terminal voltages are monitored and recorded by the UBA5 in discrete time. Each test starts when the cell is fully charged (assumed to be 100% SOC), and ends when the cell terminal voltage reaches recommended cut-off voltage 2.5V (assumed to be 0% SOC). Figure 4.2 shows the UBA5 testing interface window. In this figure, the blue line represents the input discharging pulsing currents; the black line represents the cell terminal voltages; and the magenta line represents the cell temperatures.
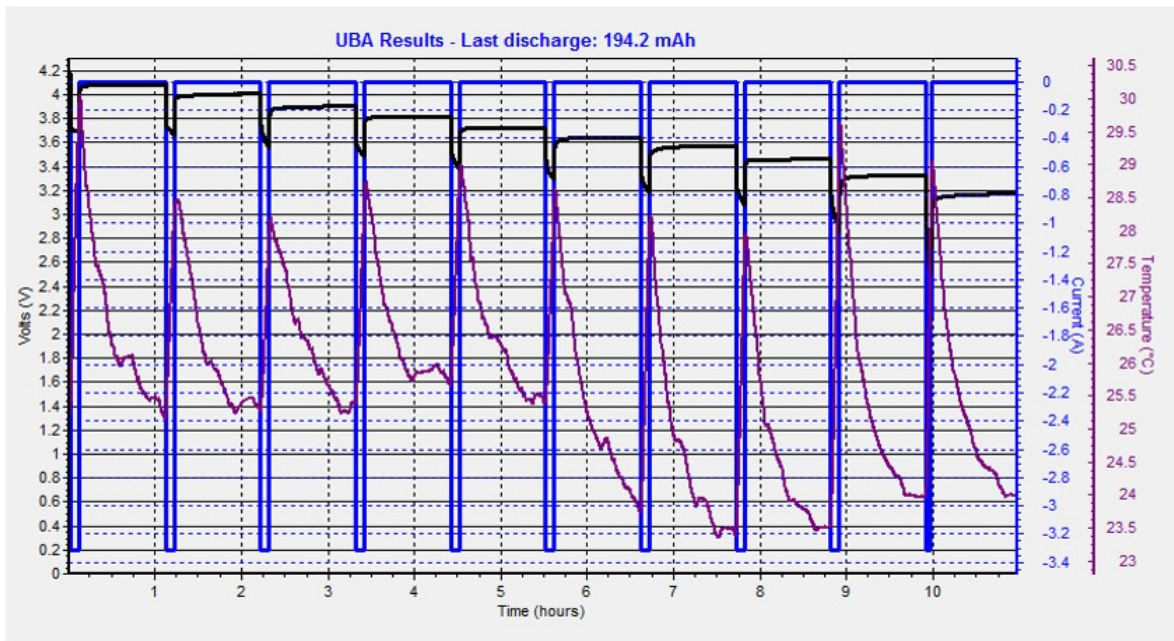
Figure 4.2 Vencon UBA5 Battery Analyzer & Charger Testing Interface.

Besides the testing interface plots shown in Figure 4.2, the test results can also be recorded into an excel datasheet. This enables the test results data to be imported into the Design Optimization Tool to estimate the cell internal parameter look-up-tables. The Design Optimization Tool then iteratively runs to optimize the parameter look-up-tables in the single cell simulation model. The optimization iteration stops when the relative sum of error squares between simulated and measured results is changing by less than the set tolerance $(1.0 * 10^{-04})$.

Figures 4.3 through 4.5 show an example of the optimization process. In all three figures, the top portion shows the terminal voltages (V) vs. time (s), and the bottom portion shows the current (I) vs. time (s).

Figure 4.3 is the example when the optimization just starts (at iteration 0). The red line (simulated terminal voltage) remains flat compared to the blue line (measured terminal voltage). This is because the parameter look-up-tables that are in the single cell simulation model are constants at this iteration (no variances at different SOC).
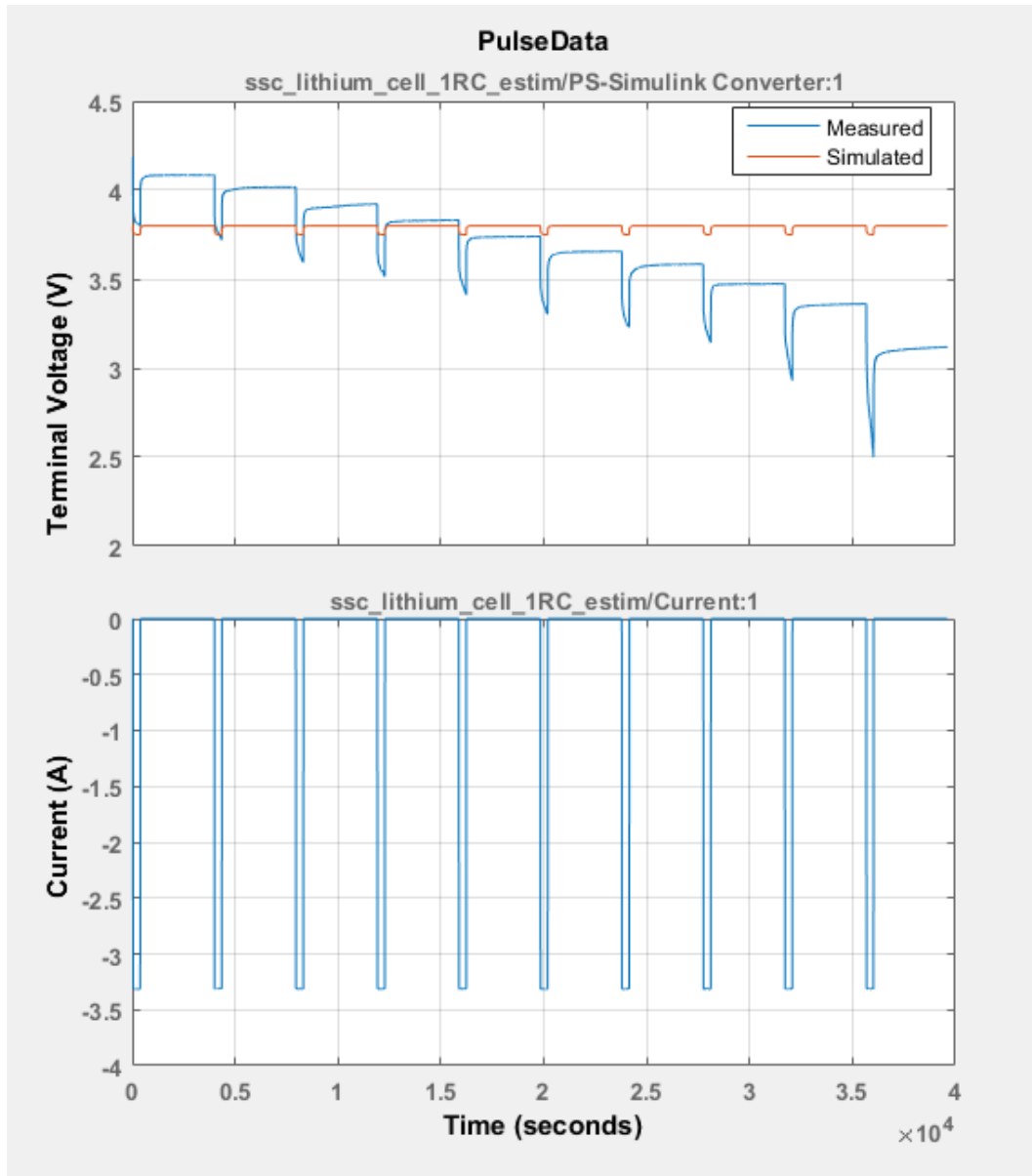
Figure 4.3 Optimization Result at Iteration 0.

Starting from iteration 1 (see Figure 4.4), the optimization tool has adjusted the parameter look-up-tables, so the simulated results come closer to the measured results compared to iteration 0.
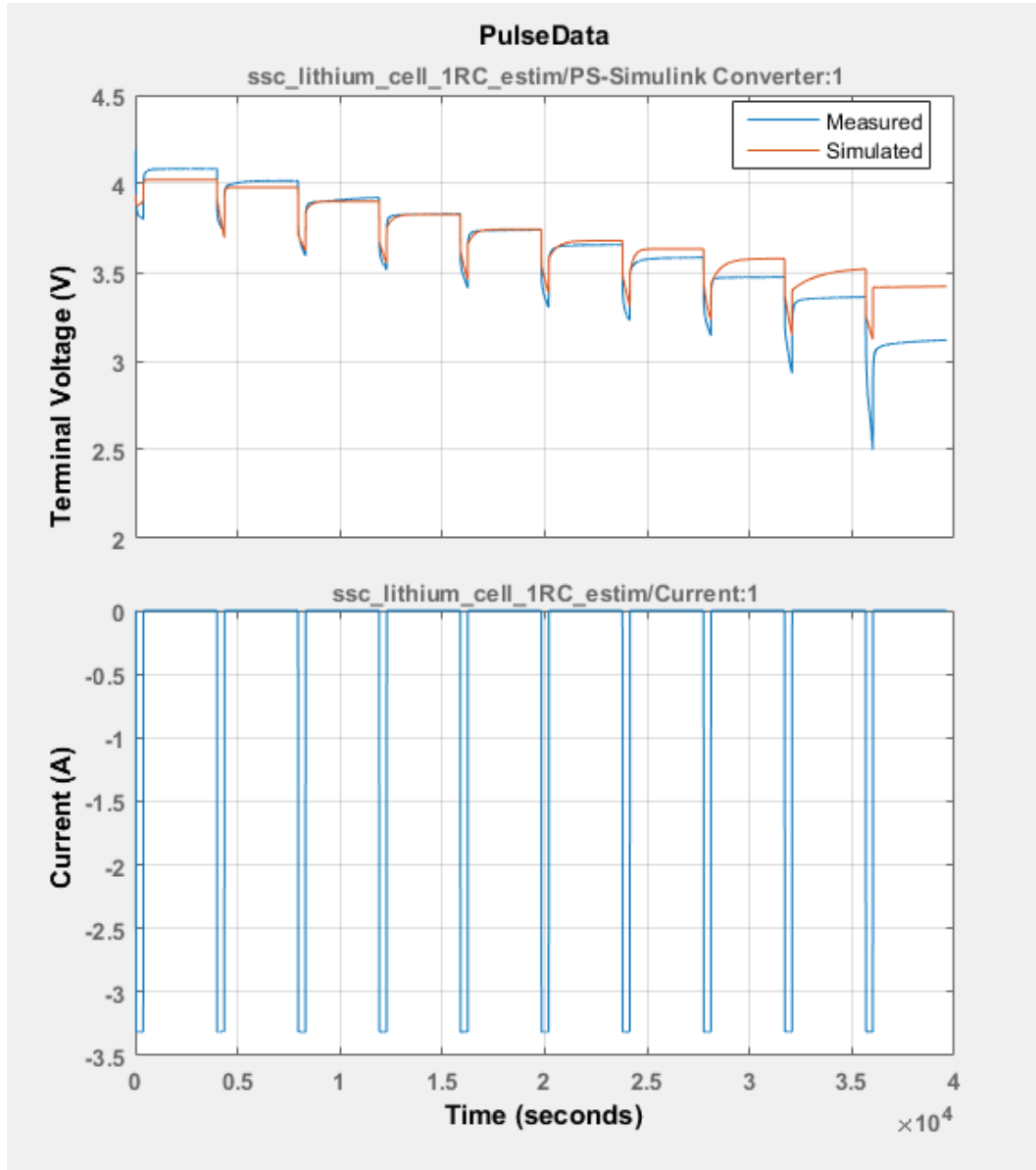
Figure 4.4 Optimization Result at Iteration 1.

Depending on the test data, it might take the Design Optimization Tool different numbers of iterations to finish the optimization. In the example shown, the optimization stops at the 15th iteration (Figure 4.5).
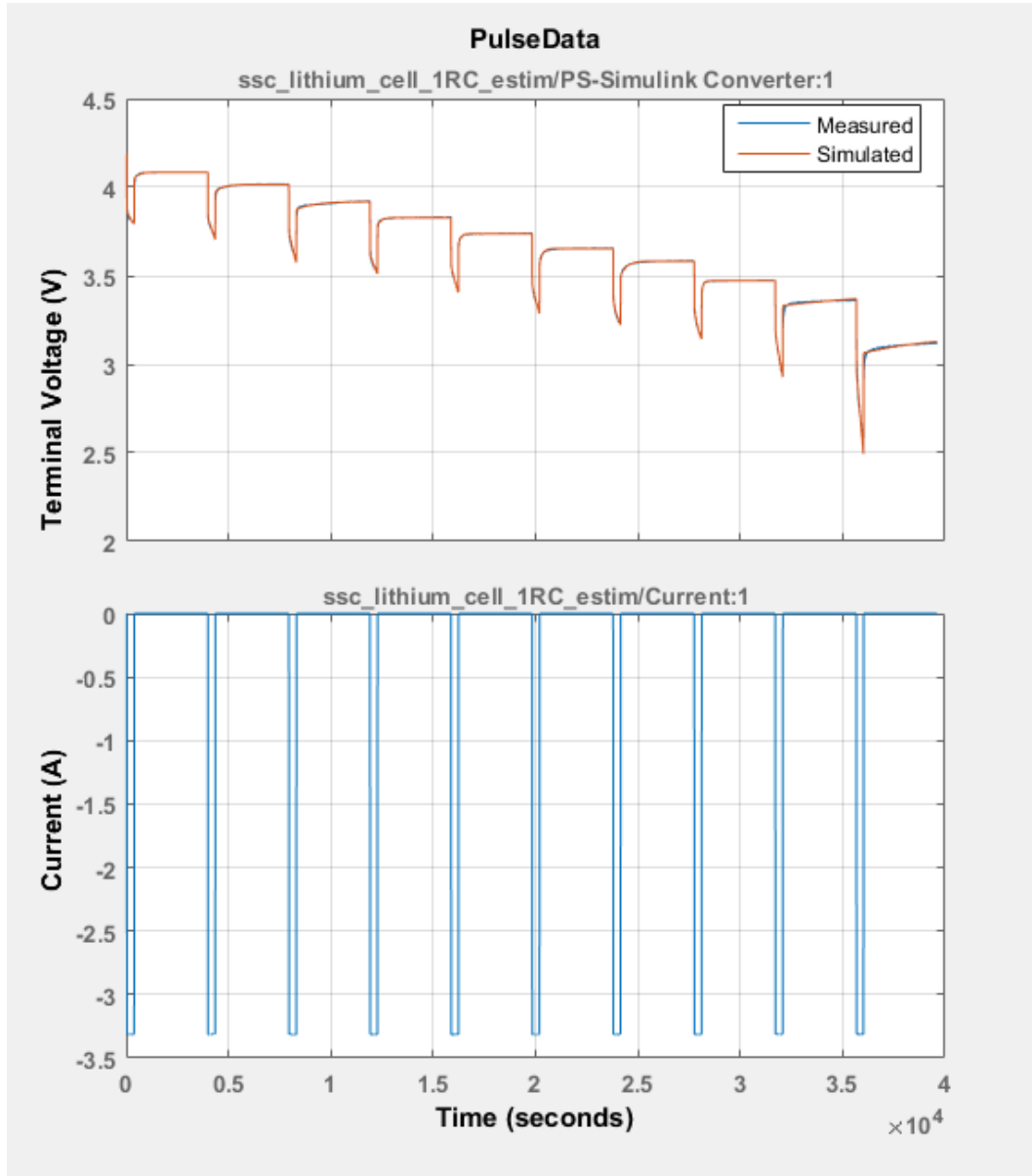
Figure 4.5 Optimization Result at Iteration 15.

To minimize the estimation errors and cell variances, 8 different NCR18650GA cells are tested. Averages of the parameter look-up-tables are used as the parameters for the single cell simulation model. Figure 4.6 through 4.9 show the averaged parameter look-up-tables.
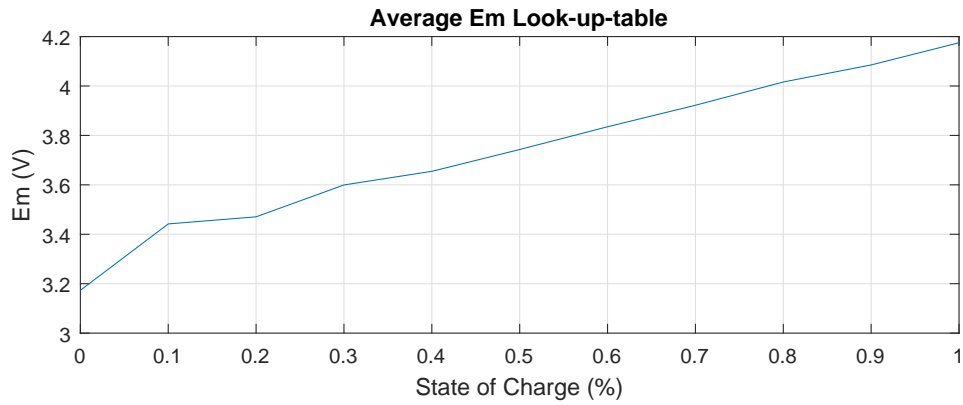
Figure 4.6 Estimated Em vs. SOC Look-up-table.
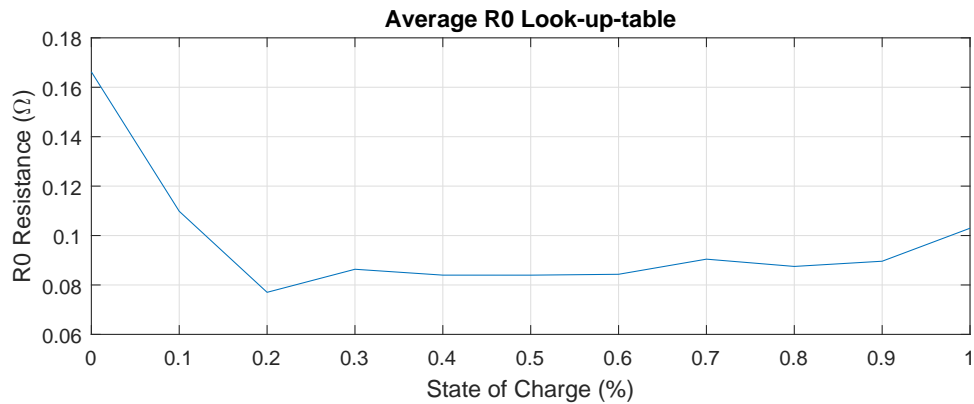
Figure 4.7 Estimated R_0 vs. SOC Look-up-table.
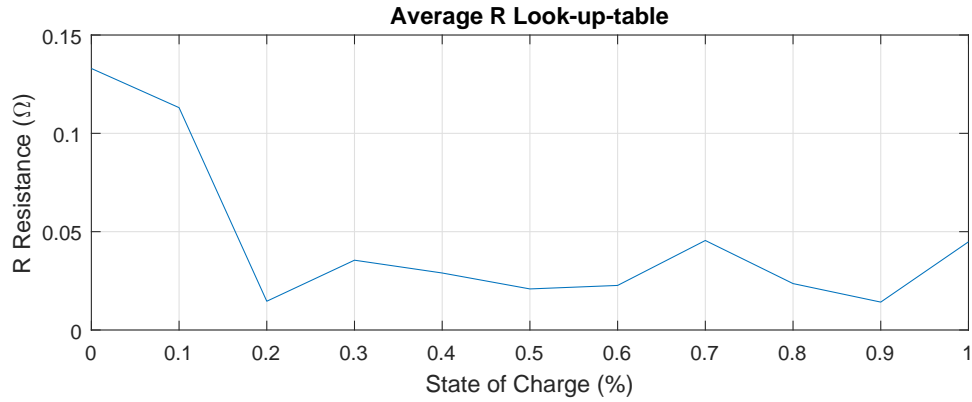
Figure 4.8 Estimated R vs. SOC Look-up-table.
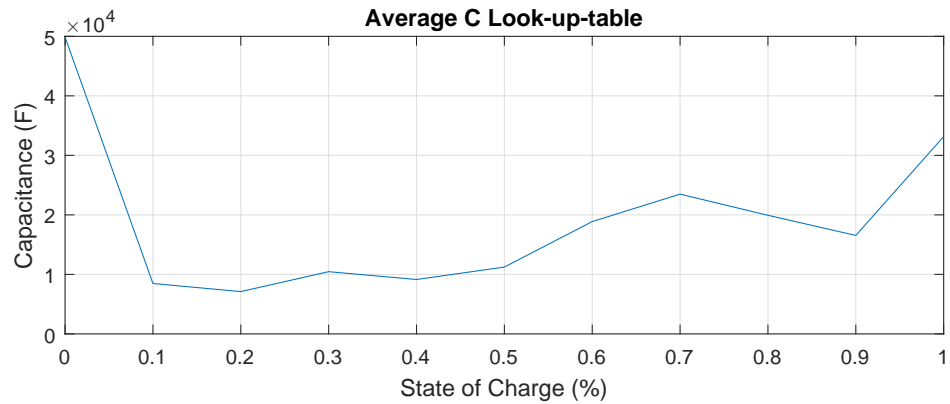
Figure 4.9 Estimated C vs. SOC Look-up-table.

The next step is to validate the single cell simulation model with the averaged parameter look-up-tables. The validation algorithm is described in Figure 4.10. First, the same discharging current profiles are inputs for both the single cell simulation model and the UBA5 battery analyzer. Then, their outputs (terminal voltages) from the simulation model and the UBA5 are compared in order to obtain the absolute and relative errors at each time step. Last, the average of the relative errors will be regarded as the simulation model error.
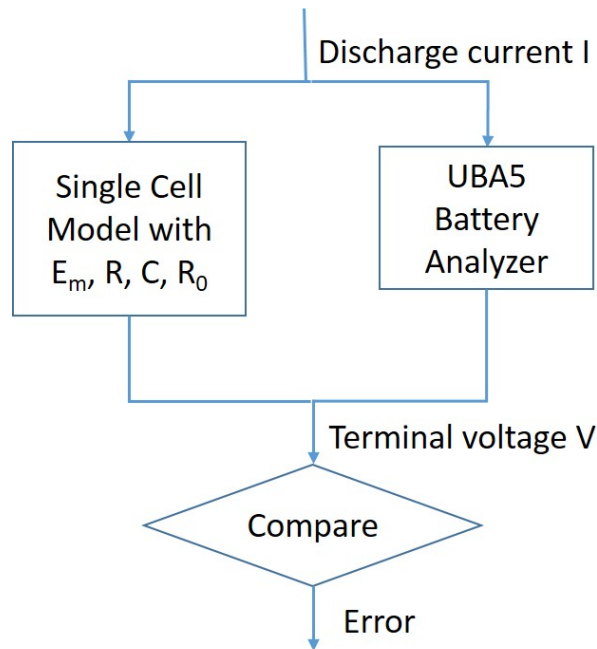
Figure 4.10 Single Cell Simulation Model Validation Algorithm.

Two discharging current profiles are used to validate the single cell simulation model:

- 3.3A (1C) constant discharging

- HK-36 flight profile: 8A constant discharging for 5 mins (simulating full-power take-off current), followed by 1.6A constant discharging (simulating cruising current)

The first validation results are plotted in Figure 4.11. The blue line shows the experimental results, and the red line shows the simulated results. The yellow line represents the absolute error between the experimental and estimated results. The average relative error of this validation profile is evaluated at 1.24%.
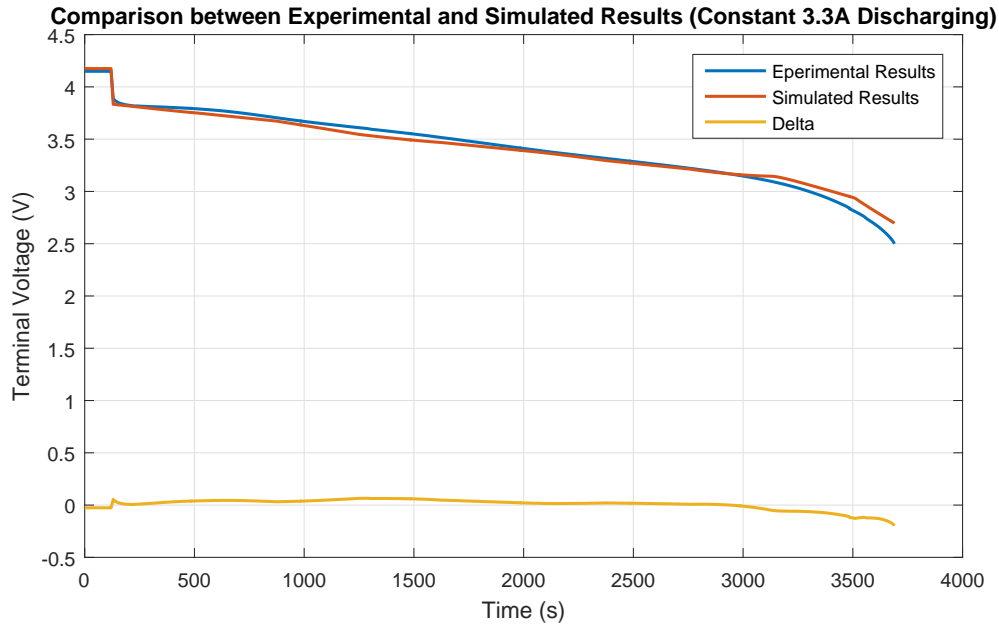
Figure 4.11 Comparison between Experimental and Simulated Results at Constant 3.3A Discharging.

The second validation results are plotted in Figure 4.12. Unlike the first constant current discharging profile, the second profile pulls the maximum allowable current from the cell first, then reduces the current to 20% of the take-off current until the recommended cut-off voltage 2.5V is reached. The overall average relative error of this validation profile is evaluated at 0.96%. Note that in this validation case, the first discharging period (8A constant discharging) has relatively larger errors compared to the second period (1.6A constant discharging). This may be caused by the heat accumulation inside of the cell during 8A discharging. When Li-ion cells are discharged at a higher current, the cell's internal impedance (or resistance) will cause the cells to generate comparatively more heat than that discharged at a lower current. The experimental results from UBA5 recorded that the cell temperature increased to

40^oC while being discharged at 8A current. However, this single cell simulation model parameter look-up-tables are estimated at 25^oC. Therefore, it is expected that the simulation accuracy decreases at 8A discharging.
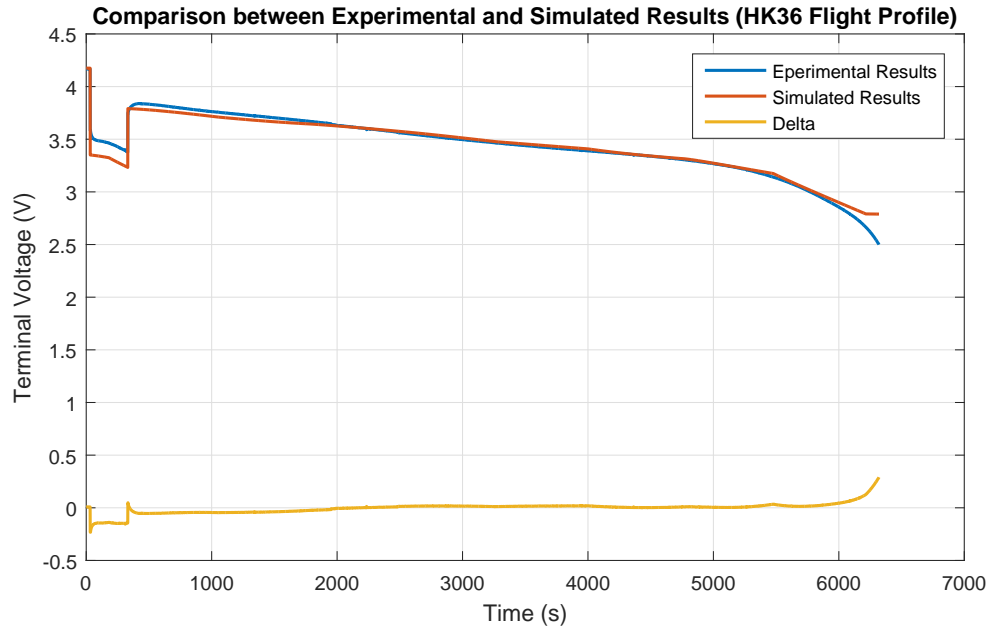
Figure 4.12 Comparison between Experimental and Simulated Results at HK-36 Flight Profile discharging.

From the two validation results, it can be seen that the average relative errors under two different discharging profiles are both below 1.5%. It can be concluded that the single cell simulation model is valid to simulate the NCR18650GA single cell behavior while being discharged at 25^oC. The model then can be used to collect the system excitation information for RLS estimator and further validate the RLS based in-flight SOC and SOH estimation algorithm. However, the simulation model has some limitations. The modified model does not include any cell internal thermal behavior, nor does it consider the heat exchange with the ambient environment.

Additionally, the parameter look-up-tables are only estimated for discharging condition. Therefore, the single cell simulation model is only valid to simulate the cell discharging behavior at 25^oC ambient temperature.

Although the above limitations exist in this simulation model, they can be overcome by repeating the same parameter estimation process using the Design Optimization Tool with experimental data under other test conditions. Similarly, the model can be further modified to fit other types of Li-ion batteries except for the NCR18650GA cells.

4.2   Recursive Least Squares (RLS) Convergence

4.2.1   RLS Based Estimation Algorithm

The RLS based in-flight SOC, SOH, and remaining energy estimations algorithm is modeled in Simulink®. Figure 4.13 shows the algorithm's main logic in Simulink interface.

The most left side of Figure 4.13 is the block for inputing the system excitation information $\underline{f}(n) = [1 \; \dot{V}(n) \; \dot{I}(n) \; I(n)]$. The second left block "RLS" runs the recursive least squares loops. The output from the RLS block – estimated parameters vector $\underline{b}(n)$ – is then fed into the algebraic calculation block "Parameters" to find the four parameters of interest (E_m, R_0, R, and C,). The E_m information will go through OCV-SOC look-up-table to estimate SOC; while the R_0 value goes through
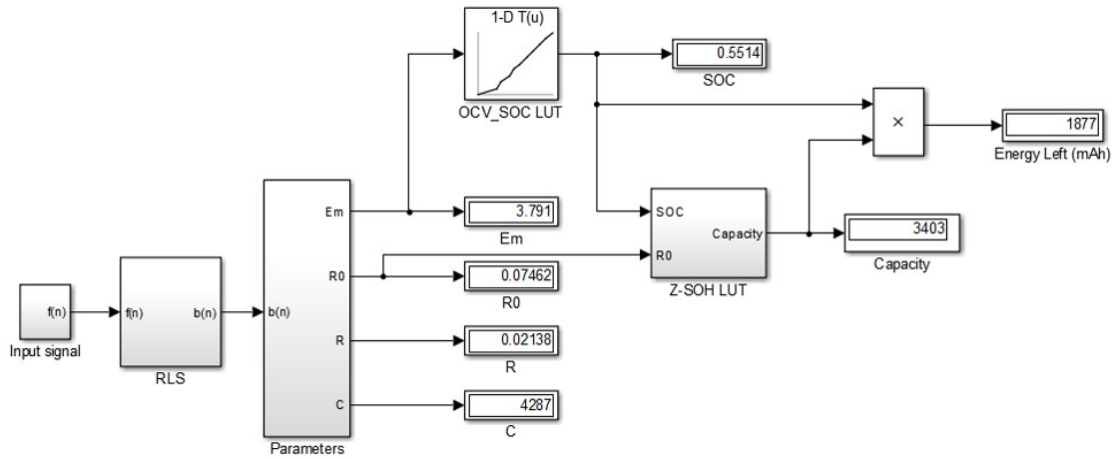
Figure 4.13 RLS Based In-Flight SOC, SOH, and the Remaining Energy Estimation Algorithm.

Z-SOH look-up-table to estimated the actual capacity of the cell. By multiplying the estimated SOC with the cell's actual capacity, the energy left inside of a cell at that moment can be evaluated.

According to the impedance (Z) equation (repeated in Equation 4.1), both R_0 and R values are needed to calculate the cell impedance.

$$Z = R(1 - e^{-\frac{1}{RC}t}) + R_0 \tag{4.1}$$

However, it can be seen in Figure 4.13 that only the R_0 information is routed into the Z-SOH look-up-table.

From the single cell parameter estimation results, the averaged values of R and C are found to be:

$$R_{avg} = 0.045 \ \Omega; \ C_{avg} = 18932 \ F \tag{4.2}$$

The time constant for the RC parallel circuit then can be calculated in Equation 4.3:

$$\tau_{RC} = R_{avg}C_{avg} = 852 \; seconds \tag{4.3}$$

Comparatively, the RLS algorithm system excitation signal duration t_{signal} lasts about 5 seconds, which is far less than the time constant of the dynamic RC circuit τ_{RC}. From Equation 4.1, it can be seen that when time t is a small value, the entire $R(1 - e^{-\frac{1}{RC}t})$ term is close to 0. Therefore, it can be asssumed that when the system input signal duration t_{signal} is small, the cell impedance Z can be approximated to be R_0 (see Equation 4.4).

$$Z \approx R_0 \; (t_{signal} << \tau) \tag{4.4}$$

4.2.2 System Excitation Analysis

Recall from Section 2.5.2 that RLS is asymptotically stable and its estimation results are convergent only when the systems are persistently excited (Johnstone et al., 1982). In the example of this thesis, it means that the RLS system input signal $\underline{f}(n) = [1 \; \dot{V}(n) \; \dot{I}(n) \; I(n)]$ must have persistent excitation.

Square waves/pulses that are similar to the ones used in the single cell simulation model parameter estimation experiments are considered first. However, this type of excitation fails because of the derivative terms in the system input vector ($\dot{V}$ and $\dot{I}$). If square waves/pulses are used, the derivatives of pulsing edges will be infinity and cause singularities, therefore they cannot be used as RLS system excitation signals.

Sinusoidal signals are better options in this case. With sine waves, all terms in the RLS input signal vector can be measured or calculated easily in discrete time without singularities. Additionally, adding a relatively small sinusoidal current into the base discharging current brings comparatively low disruption impact to the system operation compared to pulsing signals.

Figure 4.14 shows an example of RLS system input signal with sinusoidal persistent excitation.
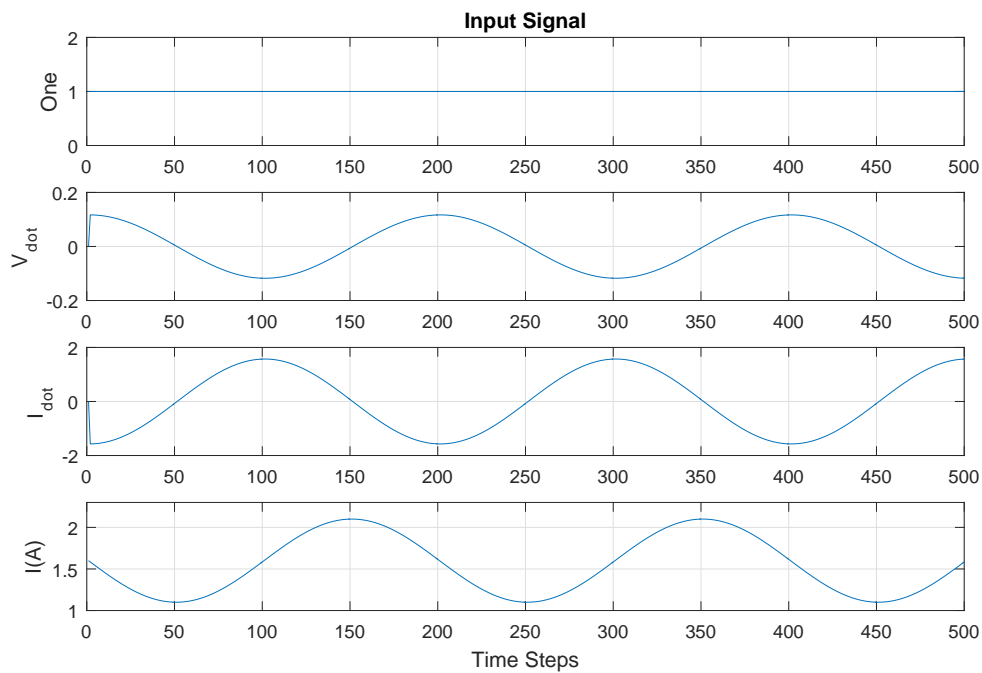
Figure 4.14 Example RLS System Input Signal with Sinusoidal Persistent Excitation.

4.2.3 RLS Validation Algorithm

Before studying how the system excitation variances affect the RLS estimation accuracy in next section, the RLS validation algorithm must be discussed. Figure 4.15 illustrates the RLS validation logic in a flow chart.
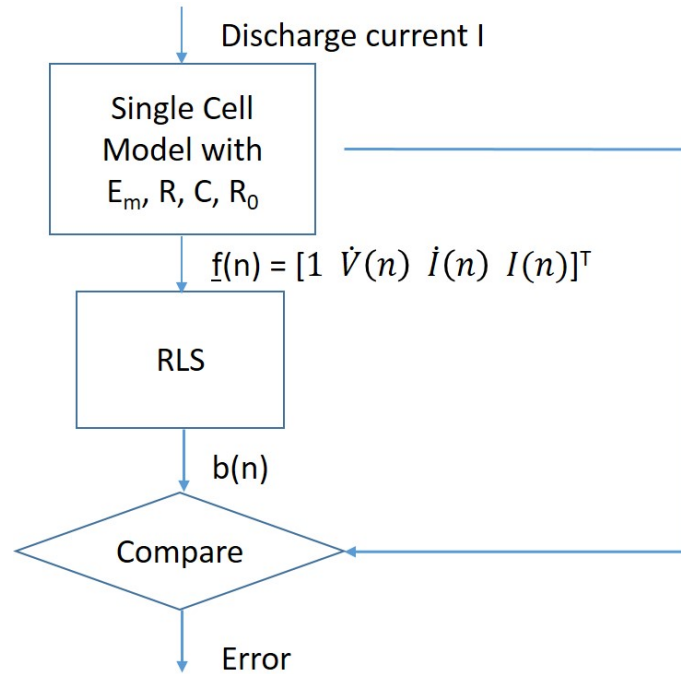
Figure 4.15 RLS Validation Algorithm.

The discharging current profile to be validated is setup as the input of the single cell simulation model. Running a simulation of the model gives the responding terminal voltages. After obtaining the currents and terminal voltages information in discrete time, the derivative terms ($\dot{V}$ and $\dot{I}$) can be calculated and the RLS system input signal $\underline{f}$ can be formed. Inputting the system excitation $\underline{f}$ into RLS is the next step. The RLS estimator then estimates the present status of the simulated cell

(including the four internal parameters, SOC, SOH, and remaining energy). Once completed with all previous steps, compare all of the estimated parameters obtained from RLS with the setup parameters in the simulation model and calculate corresponding errors of each parameter.

4.2.4   System Excitation Variance Study

Using the RLS validation algorithm, different system excitations can be sent into the RLS estimator and the estimation accuracies under different inputs can be validated.

In this section, three system excitation variances are of interest:

- Forgetting factor λ variances

- System excitation amplitude variances

- System excitation frequency variances

The forgetting factor λ variations are studied first. Tables 4.1 and 4.2 compare five validation cases where only λ is varied. All validation cases in Table 4.1 have a base discharging current of 1.6A (HK-36 cruising condition), and the sinusoidal excitation amplitude is 0.2A while Table 4.2 contains validation cases with a base discharging current of 8A (HK-36 take-off condition) and the sinusoidal excitation amplitude is 1A. The converging time $t_{converge}$ is defined as when the error e(n) stays within ± 0.001. All ten cases have the same excitation frequency of 1Hz. The simulated cell is set to be at 50% SOC.

Table 4.1 Validation Results with "Forgetting Factor" λ Variations (at 1.6 Base Current)

No.	λ	$t_{converg}$(s)	SOC Error (%)	Z Error (%)
1	0.99	3.0	0.06	0.01
2	0.95	0.9	0.12	0.01
3	0.93	0.8	0.12	0.01
4	0.9	0.7	0.14	0.01
5	0.8	0.4	0.14	0.01

Table 4.2 Validation Results with "Forgetting Factor" λ Variations (at 8A Base Current)

No.	λ	$t_{converg}$ (s)	SOC Error (%)	Z Error (%)
1	0.99	>5	1.83	0.02
2	0.95	0.9	1.94	0.02
3	0.93	0.8	0.40	0.02
4	0.9	0.7	1.13	0.04
5	0.8	0.4	0.56	0.02

From the validation cases in Tables 4.1 and 4.2, it can be seen that λ has a direct impact on the system convergence rate. The smaller λ is, the faster the system converges. At the same time, λ causes small changes in the SOC and impedance

estimation accuracies. However, the changes do not show an obvious trend with an optimizing λ that gives the best SOC and impedance accuracies.

It needs to be pointed out that even though it is ideal to have a faster converging rate for the estimation algorithm, there is a threshold of λ after which the estimation is not valid. The turning point varies depending on different system input excitation signals. For the cases validated in Tables 4.1 and 4.2, the turning point happens around $\lambda = 0.9$. When $\lambda < 0.9$, the parameters plots show abnormal data after converging (see Figure 4.16 as an example). To avoid this abnormal data, λ cannot be set to be smaller than this threshold (0.9). Additionally, for the validation cases where converging time is less than one second, both Tables 4.1 and 4.2 show an minimum SOC and impedance error at $\lambda = 0.93$.
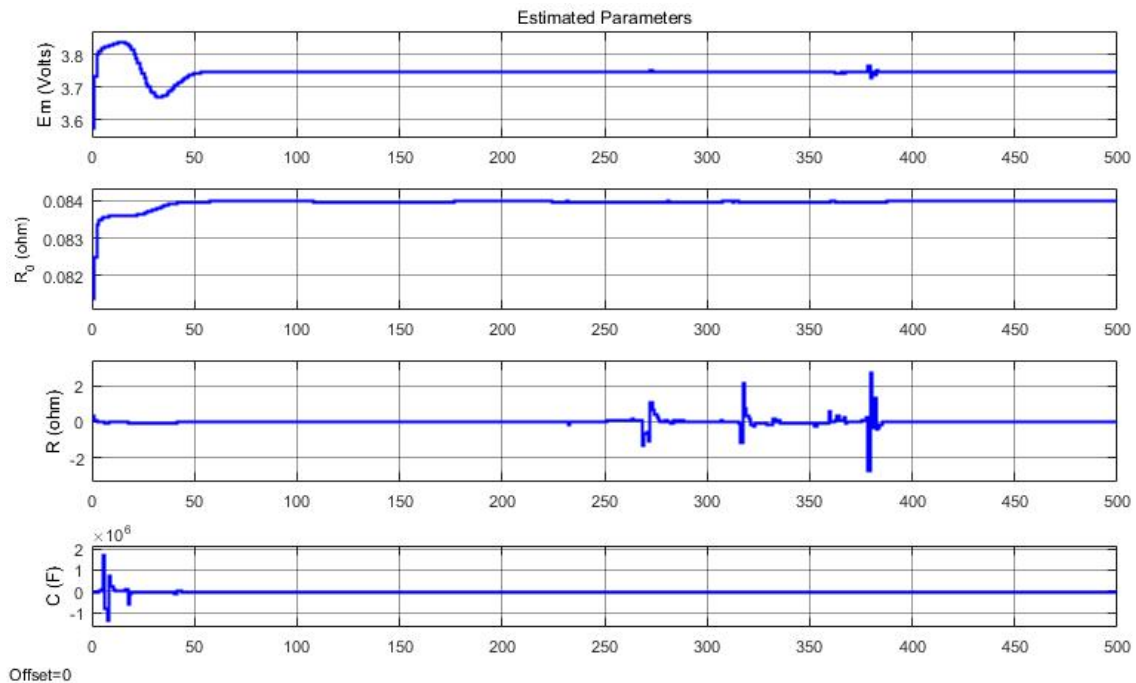
Figure 4.16 Parameters with Abnormal Data After Converged.

The sinusoidal excitation amplitude variations are studied next. Similar to the λ study cases, Table 4.3 and Table 4.4 each compares five validation cases where only the sinusoidal excitation amplitude is varied. All ten validation cases are evaluated at $\lambda = 0.93$ and 1Hz.

Table 4.3 Validation Results with Amplitude Variations (at 1.6A Base Current)

No.	Amplitude (A)	$t_{converg}$ (s)	SOC Error (%)	Z Error (%)
1	1	0.8s	0.10	0.01
2	0.5	0.8s	0.14	0.01
3	0.2	0.8s	0.12	0.01
4	0.05	0.9s	0.04	0.00
5	0.01	1.0s	0.02	0.00

Table 4.4 Validation Results with Amplitude Variations (at 8A Base Current)

No.	Amplitude (A)	$t_{converg}$ (s)	SOC Error (%)	Z Error (%)
1	2	0.9s	1.07	0.02
2	1.5	0.8s	0.38	0.01
3	1	0.8s	0.40	0.02
4	0.5	0.8s	0.44	0.02
5	0.2	0.9s	3.04	0.07

By comparing Tables 4.3 and 4.4, it can be found that for different base discharging currents, the required excitation amplitudes to achieve convergence are different. Generally speaking, larger base currents require relatively larger excitation amplitudes. In both tables, amplitude variances can be found to cause slight changes in convergence rate, SOC error, and impedance error. In 1.6A base current cases, an amplitude of 0.01A gives the best SOC and impedance estimation accuracies at the cost of relatively longer converging time. In 8A base current cases, however, an amplitude of 1.5A results in the best convergence rate, as well as SOC and impedance estimation accuracies. However, it should be noted that the amplitudes with the best estimation accuracies are not necessary in many situations. Smaller amplitudes with acceptable estimation errors and convergence rates can also be applied in order to minimize the interruption of system operation.

The sinusoidal excitation frequency variations are also studied. Table 4.5 compares six validation cases where only the sinusoidal excitation frequency is varied. Their base discharging currents are 1.6A, and their excitation amplitudes are 0.05A. Similarly, Table 4.6 compares four frequencies with a base discharging current of 8A and an excitation of 1A. All ten validation cases are evaluated at $\lambda = 0.93$.

From both Tables 4.5 and 4.6, it can be seen that 1Hz works the best for both 1.6A and 8A base current cases. However, lower frequencies with acceptable estimation errors and convergence rates can also be applied if minimum system operation interruption is desired.

Table 4.5 Validation Results with Frequency Variations (at 1.6A Base Current)

No.	Frequency (Hz)	$t_{converge}$ (s)	SOC Error (%)	Z Error (%)
1	5	0.8s	0.75%	0.02%
2	2	0.9s	0.30%	0.01%
3	1	0.9s	0.04%	0.00%
4	0.5	1.2s	0.32%	0.01%
5	0.1	0.4s	0.53%	0.14%
6	0.05	0.4s	5.01%	0.37%

Table 4.6 Validation Results with Frequency Variations (at 8A Base Current)

No.	Frequency (Hz)	$t_{converge}$ (s)	SOC Error (%)	Z Error (%)
1	5	2.8	4.62%	0.07%
2	2	0.6	0.56%	0.01%
3	1	0.8	0.40%	0.02%
4	0.5	1.0s	4.01%	0.02%

4.3   Example Case

In order to demonstrate how the SOC, SOH, and the remaining energy estimation algorithms work on a Li-ion cell, detailed step-by-step procedures will be shown in this section.

The discharging profiles with system excitations must be determined first. In this example, 1.6A base discharging current will be used to show how the estimation algorithm works using the HK-36 electric airplane cruising flight condition. A sinusoidal excitation with 0.05A amplitude and 1Hz frequency will be added on top of the base discharging current. The system input items are listed in Table 4.7.

Table 4.7 System Input Signal Key Items

Item	Value
Base Current	-1.6A
Amplitude	0.05A
Frequency	1Hz (3.14 rad/s)
Input Signal Duration	5 seconds
Step Size	0.01s (500 steps total)
SOC	50.66%
Forgetting Factor λ	0.95

All of the key items will be set up in the Li-ion single cell simulation model to get the simulated terminal voltages based on the input discharging current profile. See Figure 4.17 for simulation model set up.
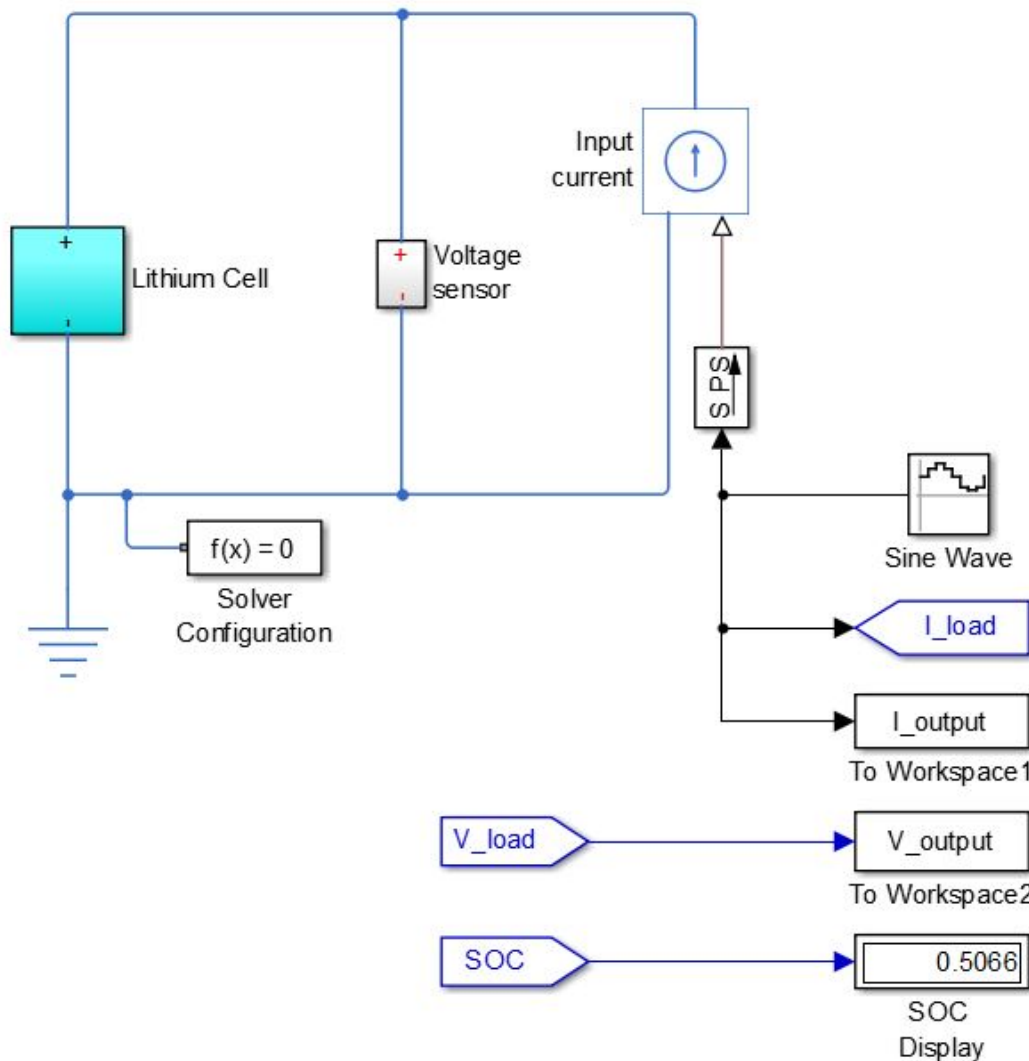
Figure 4.17 Li-ion Single Cell Simulation Model Setup.

The single cell simulation model with the setup values in Table 4.7 will produce the simulated cell terminal voltages. With the currents and terminal voltages in discrete time, the derivative terms $\dot{V}$ and $\dot{I}$ in RLS system input vectors $\underline{f}$ can be approximately calculated. The pre-determined RLS input vectors can then be concatenated into a full matrix. Figure 4.18 shows the full length of the pre-determined input signal

for the RLS estimator. Note that the pre-determined input signal matrix contains all information from beginning to end. Each row of the matrix represents one input vector at one time step. When running the RLS, only one row of the full-size matrix will be retrieved at a time in order to simulate that the RLS is running in real-time.
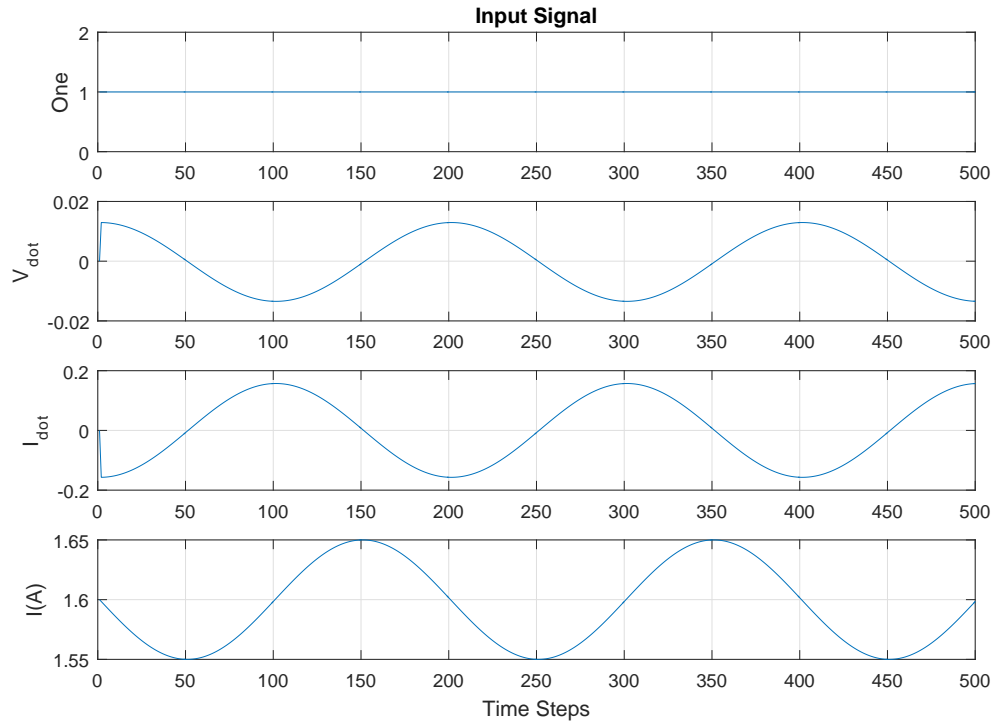
Figure 4.18 Input Signal with Excitation of the Example Case.

Figure 4.19 shows the error e(n) convergence along the time steps. Earlier in this section, the convergence of e(n) is defined when e(n) stays within 0.001. Zooming in the e(n) plot (see Figure 4.20), it can be seen that the error converges after approximately 1.5 seconds (150 time steps).
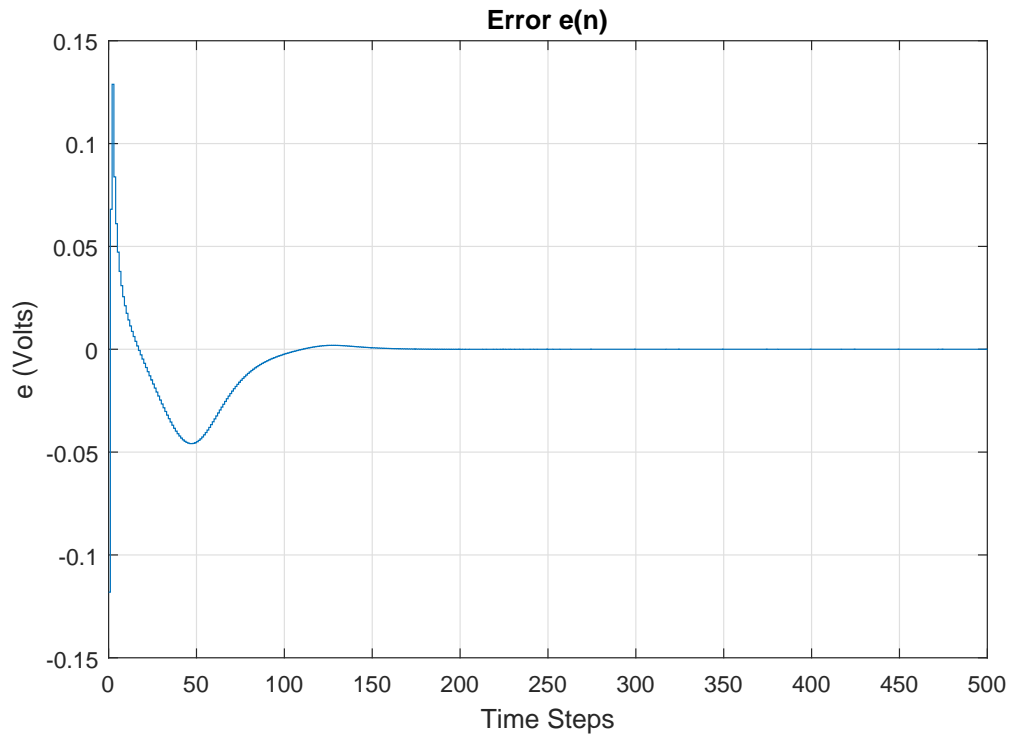
Figure 4.19 Error e(n) Convergence.
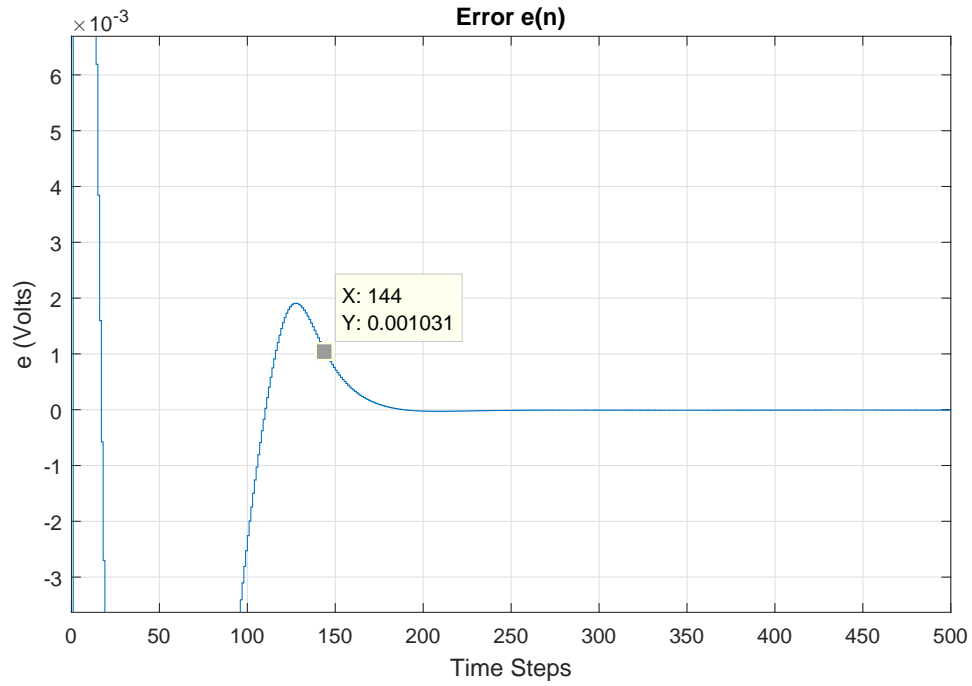
Figure 4.20 Zoomed In Error e(n) Convergence.

Figure 4.21 shows the estimated parameters' convergence. Similar to the error e(n) convergence, all four parameters achieve convergence after about 1.5 seconds (150 time steps).
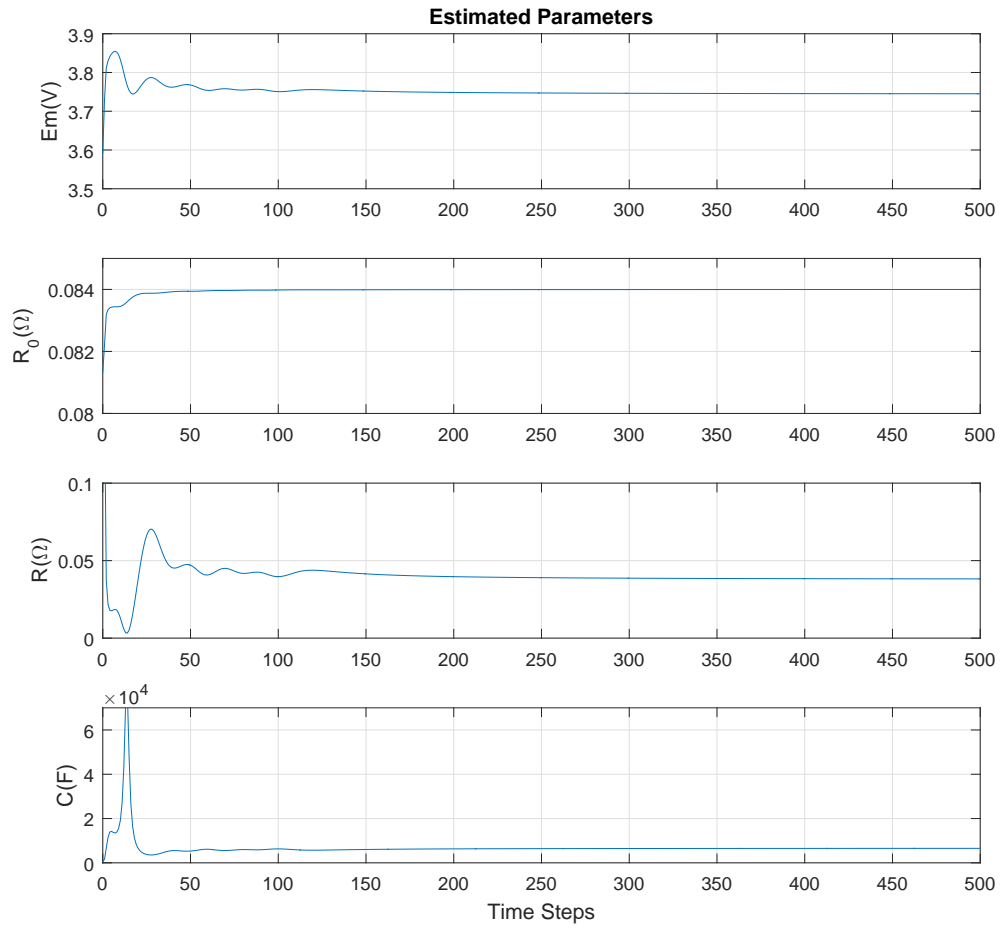
Figure 4.21 Estimated Parameters Convergence.

The validation results of this example case are listed in Table 4.8. The results show very good estimation accuracies. The SOC and impedance accuracies are under 0.1%, while the available capacity and remaining energy accuracies are around 1%.

Table 4.8 Example Case Validation Results

Item	Setup Value	Estimated Value	Error (%)
SOC (%)	50.66	50.63	0.06
Z (Ω)	0.08399	0.08400	0.01
Capacity (mAh)	3450	3417	0.96
Remaining Energy (mAh)	1750	1730	1.14

4.4 HK-36 Battery System Weight Analysis

4.4.1 Li-ion Battery Cells Weight

The Li-ion cells are the cores of the propulsive battery system since they store the electrical energy and provide the propulsive power to the motor system. In the HK-36 propulsive battery pack, a total of 2520 NCR18650GA cells are carried on board to deliver 40 HP-hr capacity. From the manufacturer datasheet, each NCR18650GA cell weighs 48g (0.106lb) (Panasonic, 2017). Therefore, the total weight of the Li-ion cells is

$$W_{Cell} = 0.106 \; lb * 2520 = 267 \; lb = 121 \; kg \tag{4.5}$$

The HK-36 battery pack's total capacity can then be calculated by Equation 4.6

$$E_{Bat} = W_{Cell} * \epsilon_{Bat} = 267 \; lb * 0.16 \text{ HP-hr/lb} = 43 \text{ HP-hr} = 32 \text{ kW-hr} \tag{4.6}$$

4.4.2 Housing Structures Weight

The HK-36 battery pack uses a translucent amber material called Ultem as the top and bottom covers of each battery module. The Ultem material in each battery module weighs 0.4 kg (0.88 lb). All of the other auxiliary structural components (such as straps and screws) for the entire 30 battery modules weigh approximately 0.5 kg (1.1 lb). Therefore, the total weight of housing structures in the battery pack can be calculated by Equation 4.7:

$$W_{House} = 0.88 \ lb * 30 + 1.1 \ lb = 28 \ lb = 13 \ kg \tag{4.7}$$

4.4.3 Cooling System Weight

The HK-36 electric airplane has a passive air-cooling system. The cooling system is composed of three parts: Phase Change Composite (PCC), cooling fins, and air ducts. The PCC material is a special graphite that absorbs the heat generated by the battery cells to prevent heat propagation among them. Cooling fins are aluminum fins or plates that transfer heat from PCC to the air flow. Air ducts are used to route the air flow that circulates around the battery modules to transfer the heat from cooling fins and BMS to external outlets.

Each battery module has one PCC brick, which weighs 0.7 kg (1.6 lb). The cooling fins, together with air ducts, weigh 7.5 kg (16.6 lb). Therefore, the HK-36 battery pack cooling system total weight is

$$W_{Cool} = 1.6 \ lb * 30 + 16.6 \ lb = 63 \ lb = 29 \ kg \tag{4.8}$$

4.4.4   BMS Weight

The BMS of HK-36 consists of all of the PCB boards that provide connectivity and management among cells within a battery module. Each battery module has three PCBs. The three PCBs, together with their mounted electric components and battery contact leaf springs, weigh 0.9 kg (2.0 lb) in total. Therefore, the total BMS weight of the entire battery pack is

$$W_{Cool} = 2.0 \ lb * 30 = 60 \ lb = 27 \ kg \tag{4.9}$$

4.4.5   Wiring Weight

The HK-36 battery pack wiring system contains all of the wires that connect battery modules in parallel and series. Depending on their functionalities and sizes, the wires can be categorized into two types.

Type 1 wires are No. 6 American wire gauge (AWG) aviation wires that connect every two battery modules in parallel. A total length of 14 ft of such wire will be used. The density of such PTFE (Teflon) insulated gauge 6 wires is 140 lb/kft (Standard Wire and Cable Co., 2017).

Type 2 wires are No. 4 AWG aviation wires that connect all battery modules in series. Approximately 200 ft of type 2 wires will be used. The density of such PTFE (Teflon) insulated gauge 4 wires is 205 lb/kft (Standard Wire and Cable Co., 2017).

The total weight of the HK-36 wiring system is calculated below:

$$W_{Wire} = 0.014 \ \text{kft} * 140 \ \text{lb/kft} + 0.2 \ \text{kft} * 205 \ \text{lb/kft} = 43 \ \text{lb} = 20 \ \text{kg} \tag{4.10}$$

4.4.6 Weight Fraction Results

Based on all of the sub-system weights, the total weight of the HK-36 propulsive system is calculated to be:

$$W_{Bat} = W_{Cell} + W_{House} + W_{Cool} + W_{BMS} + W_{Wire} = 460 \text{ lb} = 208 \text{ kg} \qquad (4.11)$$

Since the HK-36 electric airplane does not alter any aerodynamic characteristics of the airplane base structure, its MGTOW remains the same as indicated on the original aircraft's flight manual, which is 1698 lb (700kg) (Diamond Aircraft, 1997).

With each sub-system's weight, battery system weight, and aircraft's MGTOW, each sub-system's weight fraction can be calculated. Take the battery cells as an example:

Battery cell's weight fraction in relation to aircraft's MGTOW

$$w_{Cell} = \frac{267 \ lb}{1698 \ lb} * 100\% = 15.7\% \qquad (4.12)$$

Battery cell's weight fraction in relation to the propulsive battery system weight

$$w_{Cell} = \frac{267 \ lb}{460 \ lb} * 100\% = 58.0\% \qquad (4.13)$$

All of the other sub-systems weight fractions are summarized and compared in Table 4.9.

Table 4.9 HK-36 Propulsive Battery Sub-systems Weight Fractions

Sub-system	w (in relation to W_0)	w (in relation to W_{Bat})
Battery Cells	15.7%	58.0%
Housing Structures	1.6%	6.0%
Cooling System	3.7%	13.7%
BMS	3.5%	13.0%
Wires	2.5%	9.4%
Total	27.1%	100%

From Table 4.9, it can be seen that the HK-36 propulsive battery system weight takes about 27% of the aircraft's MGTOW. Among all of its sub-systems, Li-ion cells take the biggest part of weight, which is 58%. In other words, in the HK-36 propulsive battery system, only 58% of weight provides storage of energy, while the other 42% of weight goes to auxiliary components that assist the cells to deliver propulsion. Recall that NCR18650GA cells have a specific energy of 0.16 HP-hr/lb. After taking the cells weight fraction into consideration, a new "effective specific energy" can be calculated by Equation 4.14.

$$\epsilon_{Bat\_e} = 58\% * \epsilon_{Bat} = 0.58 * 0.16 \text{ HP-hr/lb} = 0.09 \text{ HP-hr/lb} = 150 \text{ W-hr/kg} \quad (4.14)$$

The propulsive battery pack's total capacity can be calculated with Equation 4.15.

$$E_{Bat} = W_0 * w_{Cell} * \epsilon_{Bat} \quad (4.15)$$

From this equation, with W_0 being a pre-determined constant, linear relationships can be obtained between two parameters while keeping the third parameter constant. Therefore, the effect of parameter variations on weight fractions can be analyzed.

By keeping the battery cells' specific energy, ϵ_{Bat}, constant at 0.16 HP-hr/lb, a linear relationship between the total capacity, E_{Bat}, and the battery cells weight fraction, w_{Cell}, can be obtained. The weight fraction of the propulsive battery system in relation to the aircraft's MGTOW can also be calculated. The purpose of this analysis is to see that based on today's Li-ion battery technology, if bigger capacity battery packs are desired, more weight of the battery system is required as a trade-off. Table 4.10 summarizes the calculated results.

Table 4.10 HK-36 Propulsive Battery Sub-systems Weight Fractions with Capacity Variations

Capacity E_{Bat} (HP-hr)	$\frac{W_{Cell}}{W_0}$	$\frac{W_{Bat}}{W_0}$
43	16%	27%
50	18%	32%
60	22%	38%
70	26%	44%

From Table 4.10, it can be estimated that based on the same design of HK-36, if the total battery pack capacity is increased to 70 HP-hr to extend the aircraft cruising endurance, the battery cells will take 26% of the aircraft's MGTOW, and the entire propulsive battery system will take 44% of the aircraft's MGTOW.

Keeping the battery pack capacity E_{Bat} at 43 HP-hr will enable the analysis between battery cells specific energy ϵ_{Bat} and the cells weight fractions. The purpose of this analysis is to show that when designing battery packs with the same capacities, the Li-ion battery technology improvement will directly help with lowering the weight fractions of propulsive battery systems. Calculation results are shown in Table 4.11.

Table 4.11 HK-36 Propulsive Battery Sub-systems Weight Fractions with Specific Energy Variations

Specific Energy ϵ_{Bat} (HP-hr/lb)	$\frac{W_{Cell}}{W_0}$	$\frac{W_{Bat}}{W_0}$
0.16	16%	27%
0.2	13%	22%
0.3	8%	15%
0.5	5%	9%

From Table 4.11, it can be estimated that based on the same design of the HK-36, if the total Li-ion battery technology improvement doubles the specific energy to 0.3 HP-hr/lb, the battery cells will take 8% of the aircraft's MGTOW, and the entire propulsive battery system will take 15% of the aircraft's MGTOW. And if the specific energy can be further increased to 0.5 HP-hr/lb, then the battery cells will take 5% of the aircraft's MGTOW, with the entire battery system only taking 9% of the aircraft's MGTOW.

5. Conclusion

5.1 Significant Results

An equivalent circuit model (ECM) of lithium-ion cells was selected to theoretically model the batteries' electrical behavior. The four internal parameter look-up-tables that describe this ECM were estimated based on the NCR18650GA cells experimental data. A lithium-ion single cell simulation model was developed to accommodate the four parameter look-up-tables. The simulation model is then able to simulate NCR18650GA battery cells behavior during discharge at 25^oC. Validations of the single cell simulation model with both constant discharging current and HK-36 flight mission profile show simulation errors less than 1.3%.

A recursive least squares (RLS) based real-time estimator was created to estimate the battery pack's SOC, SOH, and the remaining energy. It is exponentially convergent with a forgetting factor λ $(0 < \lambda \leq 1)$. Given an input signal with persistent excitation, this RLS based estimator is able to adaptively estimate one Li-ion cell's SOC, SOH, and the remaining energy in real time. The algorithm can also estimate a battery pack's remaining energy assuming that all cells connected in parallel are identical. The validation results indicate that the RLS based estimator achieves convergence within a very short time period (≈ 1 second) with desirable estimation accuracy (normally under 1%). Additionally, the RLS based estimator can be applied

to any type or configuration of battery packs provided that OCV-SOC and Z-SOH relations can be pre-determined.

The HK-36 propulsive battery system takes approximately 27% of the aircraft gross weight. 58% of the battery system weight is the cells weight, and 42% is the auxiliary components weight. Taking the weight fraction into consideration, NCR18650GA cells effective specific energy reduces from 0.16 HP-hr/lb (259 W-hr/kg) to 0.09 HP-hr/lb (150 W-hr/kg).

5.2   Future Work

The lithium-ion single cell simulation model developed in this thesis excludes any thermal behavior of cells or any heat exchange with the ambient environment. Future work should be done to expand the 2D parameter look-up-tables to 3D to include the thermal effects by adding a third temperature axis.

Li-ion batteries have different performances when being charged and discharged. In this thesis, all battery performance plots and internal parameter look-up-tables are obtained in situations when the cells are being discharged. Future work would include the battery charging performance by repeating the same experiments discussed in this thesis, but under situations when the cells are being charged.

At the beginning of this thesis, the assumption is made that all cells connected in parallel are identical. However, in real world cases, variations exist among cells in parallel. This could result in different current splits and cause remaining energy

imbalances among them. To solve this problem, parameter variations among parallel connected cells would be considered in future work.

From the input signal variations analysis in this research, no optimized excitation amplitudes or frequencies were discovered, even though some excitations had better estimation accuracies than others. More combinations of excitation amplitudes and frequencies can be compared and analyzed in future work to determine how input signal variances affect estimation accuracies.

Future research could also be done to decide if it is feasible to use the current ripple from the motor controller caused by transistor switching as the system persistent excitation for RLS estimation algorithm.

REFERENCES

Balas, M. (2017). *Least squares notes.*

Battery Bro. (2014, September). *Inspecting the new panasonic-sanyo ncr18650bf.* Retrieved August, 2017, from `https://batterybro.com/blogs/18650-wholesale-battery-reviews/17840447-awesome-batteries-part-1-inspecting-the-new-panasonic-sanyo-ncr18650bf`

Birkl, C. R., Roberts, M. R., McTurk, E., Bruce, P. G., & Howey, D. A. (2017, December). Degradation diagnostics for lithium ion cells. *Journal of Power Sources*, *341*, 373-386. Retrieved from `http://www.sciencedirect.com/science/article/pii/S0378775316316998`

Chaoui, H., Golbon, N., Hmouz, I., Souissi, R., & Tahar, S. (2015, March). Lyapunov-based adaptive state of charge and state of health estimation for lithium-ion batteries. *IEEE Transactions on Industrial Electronics*, *62*(3), 1610-1618. doi: 10.1109/TIE.2014.2341576

Chevron Products Company. (2007). *Aviation fuels technical review.* Retrieved August, 2017, from `https://www.cgabusinessdesk.com/document/aviation_tech_review.pdf`

Diamond Aircraft. (1997, Mar). *Airplane flight manual for the powered sailplane hk 36 ttc.* Diamond Aircraft.

Gholizadeh, M., & Salmasi, F. R. (2014, March). Estimation of state of charge, unknown nonlinearities, and state of health of a lithium-ion battery based on a comprehensive unobservable model. *IEEE Transactions on Industrial Electronics*, *61*(3), 1335-1344. doi: 10.1109/TIE.2013.2259779

Gibbs, B. P. (2011). *Advanced kalman filtering, least-squares and modeling: A practical handbook* (1st ed.). Wiley.

He, H., Xiong, R., & Fan, J. (2011, March). Evaluation of lithium-ion battery equivalent circuit models for state of charge estimation by an experimental approach. *Energies*, *4*, 582-598. doi: 10.3390/en4040582

Huang, W., & Qahouq, J. A. A. (2014, November). An online battery impedance measurement method using dcdc power converter control. *IEEE Transactions on Industrial Electronics*, *61*(11), 5987-5995. doi: 10.1109/TIE.2014.2311389

Huria, T., Ceraolo, M., Gazzarri, J., & Jackey, R. (2012). High fidelity electrical model with thermal dependence for characterization and simulation of high power lithium battery cells. *2012 IEEE International Electric Vehicle Conference*, 1-8. doi: 10.1109/IEVC.2012.6183271

Johnstone, R. M., Johnson, C. R., Bitmead, R. R., & Anderson, B. D. O. (1982). Exponential convergence of recursive least squares with exponential forgetting factor. *21st IEEE Conference on Decision and Control, Orlando, FL*, 994-997. doi: 10.1109/CDC.1982.268295

Karden, E., Buller, S., & Doncker, R. W. D. (2000). A method for measurement and interpretation of impedance spectra for industrial batteries. *Journal of Power Sources*, *85*, 72-78. Retrieved from `http://www.sciencedirect.com/science/article/pii/S0378775399003857`

Lee, S., Kim, J., Lee, J., & B.H.Cho. (2008). State-of-charge and capacity estimation of lithium-ion battery using a new open-circuit voltage versus state-of-charge. *Journal of Power Sources*, *185*, 1367-1373. Retrieved from `http://www.sciencedirect.com/science/article/pii/S0378775308017965`

Panasonic. (2017). *Specifications for ncr18650ga.* Retrieved July, 2017, from `https://www.nkon.nl/sk/k/ncr18650ga.pdf`

Rowell, D. (2008, Fall). *2.161 signal processing: Continuous and discrete.* Retrieved from `http://ocw.mit.edu`

Shell. (1999, February). *Shell avgas 100ll piston engine aircraft fuel.* Retrieved August, 2017, from `http://www.shell.com.au/motorists/shell-fuels/msds-tds/_jcr_content/par /textimage_278c.stream/1468561712721 /42cc39fc0b31146bc1c4d344c08422206521206f80d031b5f89f9b697c327c81 /avgas-100ll-pds.pdf`

Snihir, I., Rey, W., Verbitskiy, E., Belfadhel-Ayeb, A., & Notten, P. H. (2006). Battery open-circuit voltage estimation by a method of statistical analysis. *Journal of Power Sources*, *159*, 1484-1487. Retrieved from `http://www.sciencedirect.com/science/article/pii/S0378775305016460`

Standard Wire and Cable Co. (2017). *Technical handbook and catalog* (12th ed.). Retrieved August,2017, from `http://www.standard-wire.com/downloads/swc_catalog.pdf`

Stroe, D.-I., Swierczynski, M., Kr, S. K., & Teodorescu, R. (2016). A comprehensive study on the degradation of lithium-ion batteries during calendar ageing: The internal resistance increase. *2016 IEEE Energy Conversion Congress and Exposition (ECCE), Milwaukee, WI, 2016*, 1-7. doi: 10.1109/ECCE.2016.7854664

Tripathy, Y., McGordon, A., Marco, J., & Gama-Valdez, M. (2014). State-of-charge estimation algorithms and their implications on cells in parallel. *2014 IEEE International Electric Vehicle Conference (IEVC), Florence, 2014*, 1-6. doi: 10.1109/IEVC.2014.7056168

United States Energy Information Administration. (2017, June). *Monthly energy review june 2017. table 3.7c petroleum consumption: Transportation and electric power sectors.* Retrieved from `https://www.eia.gov/totalenergy/data/monthly/pdf/sec3_21.pdf`

United States Federal Aviation Administration. (2017). *Faa aerospace forecast (fiscal years 2017-2037).* Retrieved July, 2017, from `https://www.faa.gov/data_research/aviation/aerospace_forecasts/media /FY2017-37_FAA_Aerospace_Forecast.pdf`

Xiong, R., Sun, F., Gong, X., & He, H. (2013). Adaptive state of charge estimator for lithium-ion cells series battery pack in electric vehicles. *Journal of Power Sources*, *242*, 699-713. Retrieved from http://www.sciencedirect.com/science/article/pii/S0378775313008616

YASA Motors. (2017). *Yasa 750.* Retrieved July, 2017, from http://www.yasamotors.com/wp-content/uploads/2014/07/Datasheet-YASA-750_en-ID-15637.pdf